



This is a repository copy of *The double tidal disruption event AT 2022dbl implies that at least some “standard” optical tidal disruption events are partial disruptions.*

White Rose Research Online URL for this paper:

<https://eprints.whiterose.ac.uk/228840/>

Version: Published Version

Article:

Makrygianni, L. orcid.org/0000-0002-7466-4868, Arcavi, I. orcid.org/0000-0001-7090-4898, Newsome, M. orcid.org/0000-0001-9570-0584 et al. (37 more authors) (2025) The double tidal disruption event AT 2022dbl implies that at least some “standard” optical tidal disruption events are partial disruptions. *The Astrophysical Journal Letters*, 987 (1). L20. ISSN 2041-8205

<https://doi.org/10.3847/2041-8213/ade155>

Reuse

This article is distributed under the terms of the Creative Commons Attribution (CC BY) licence. This licence allows you to distribute, remix, tweak, and build upon the work, even commercially, as long as you credit the authors for the original work. More information and the full terms of the licence here:

<https://creativecommons.org/licenses/>

Takedown

If you consider content in White Rose Research Online to be in breach of UK law, please notify us by emailing eprints@whiterose.ac.uk including the URL of the record and the reason for the withdrawal request.



eprints@whiterose.ac.uk
<https://eprints.whiterose.ac.uk/>



The Double Tidal Disruption Event AT 2022dbl Implies that at Least Some “Standard” Optical Tidal Disruption Events Are Partial Disruptions

Lydia Makrygianni^{1,2} , Iair Arcavi¹ , Megan Newsome^{3,4} , Ananya Bandopadhyay⁵ , Eric R. Coughlin⁵ , Itai Linial^{6,7} , Brenna Mockler⁸ , Eliot Quataert⁹ , Chris Nixon¹⁰ , Benjamin Godson¹¹ , Miika Pursiainen¹¹ , Giorgos Leloudas¹² , K. Decker French¹³ , Adi Zitrin¹⁴ , Sara Faris¹ , Marco C. Lam¹⁵ , Assaf Horesh¹⁶ , Itai Sfaradi¹⁶ , Michael Fausnaugh¹⁷ , Ehud Nakar¹ , Kendall Ackley¹¹ , Moira Andrews^{3,4} , Panos Charalampopoulos¹⁸ , Benjamin D. R. Davies^{11,19} , Yael Dgany¹ , Martin J. Dyer²⁰ , Joseph Farah^{3,4} , Rob Fender²¹ , David A. Green²² , D. Andrew Howell^{3,4} , Thomas Killestein¹⁸ , Niilo Koivisto¹⁸ , Joseph Lyman¹¹ , Curtis McCully³ , Morgan A. Mitchell^{11,19} , Estefania Padilla Gonzalez^{3,4} , Lauren Rhodes²¹ , Anwasha Sahu¹¹ , Giacomo Terreran^{3,4} , and Ben Warwick¹¹ 

¹The School of Physics and Astronomy, Tel Aviv University, Tel Aviv 69978, Israel; lydiamakr@gmail.com

²Department of Physics, Lancaster University, Lancaster LA1 4YB, UK

³Las Cumbres Observatory, Goleta, CA 93117, USA

⁴Department of Physics, University of California, Santa Barbara, CA 93106, USA

⁵Department of Physics, Syracuse University, Syracuse, NY 13210, USA

⁶Columbia Astrophysics Laboratory, Columbia University, New York, NY 10027, USA

⁷School of Natural Sciences, Institute for Advanced Study, Princeton, NJ 08540, USA

⁸The Observatories of the Carnegie Institution for Science, Pasadena, CA 91101, USA

⁹Department of Astrophysical Sciences, Princeton University, Peyton Hall, Princeton, NJ 08540, USA

¹⁰School of Physics and Astronomy, Sir William Henry Bragg Building, Woodhouse Lane, University of Leeds, Leeds LS2 9JT, UK

¹¹Department of Physics, University of Warwick, Gibbet Hill Road, Coventry, CV 4 7AL, UK

¹²DTU Space, National Space Institute, Technical University of Denmark, Elektrovej 327, 2800, Kgs. Lyngby, Denmark

¹³Department of Astronomy, University of Illinois, 1002 West Green Street, Urbana, IL 61801, USA

¹⁴Physics Department, Ben-Gurion University of the Negev, PO Box 653, Be'er-Sheva 8410501, Israel

¹⁵Institute for Astronomy, University of Edinburgh, Royal Observatory, Blackford Hill, Edinburgh EH9 3HJ, UK

¹⁶Racah Institute of Physics, The Hebrew University of Jerusalem, Jerusalem 91904, Israel

¹⁷Department of Physics & Astronomy, Texas Tech University, Lubbock, TX 79409-1051, USA

¹⁸Department of Physics and Astronomy, University of Turku, FI-20014 Turku, Finland

¹⁹Center for Exoplanets and Habitability, University of Warwick, Gibbet Hill Road, Coventry CV 4 7AL, UK

²⁰Department of Physics and Astronomy, University of Sheffield, Sheffield, S3 7RH, UK

²¹Astrophysics, Department of Physics, University of Oxford, Keble Road, Oxford OX1 3RH, UK

²²Astrophysics Group, Cavendish Laboratory, 19 J.J. Thomson Avenue, Cambridge CB3 0HE, UK

Received 2025 March 28; revised 2025 May 9; accepted 2025 May 20; published 2025 July 1

Abstract

Flares produced following the tidal disruption of stars by supermassive black holes can reveal the properties of the otherwise dormant majority of black holes and the physics of accretion. In the past decade, a class of optical-ultraviolet tidal disruption flares has been discovered whose emission properties do not match theoretical predictions. This has led to extensive efforts to model the dynamics and emission mechanisms of optical-ultraviolet tidal disruptions in order to establish them as probes of supermassive black holes. Here we present the optical-ultraviolet tidal disruption event AT 2022dbl, which showed a nearly identical repetition 700 days after the first flare. Ruling out gravitational lensing and two chance unrelated disruptions, we conclude that at least the first flare represents the partial disruption of a star, possibly captured through the Hills mechanism. Since both flares are typical of the optical-ultraviolet class of tidal disruptions in terms of their radiated energy, temperature, luminosity, and spectral features, it follows that either the entire class are partial rather than full stellar disruptions, contrary to the prevalent assumption, or some members of the class are partial disruptions, having nearly the same observational characteristics as full disruptions. Whichever option is true, these findings could require revised models for the emission mechanisms of optical-ultraviolet tidal disruption flares and a reassessment of their expected rates.

Unified Astronomy Thesaurus concepts: [Black hole physics \(159\)](#); [Tidal disruption \(1696\)](#); [Black holes \(162\)](#)

Materials only available in the [online version of record](#): machine-readable table

1. Introduction

After a star is torn apart by the tidal forces of a supermassive black hole (SMBH) in what is known as a tidal disruption event (TDE), typically half of its mass will be bound to the black hole

and half will be ejected (J. H. Lacy et al. 1982; M. J. Rees 1988). For SMBH masses $\lesssim 10^8 M_\odot$ (with the exact threshold depending on the spin of the SMBH), the disruption of a Sun-like star will occur outside the event horizon, producing an observable flare. Such flares can reveal the properties of the otherwise dormant majority of black holes and the physics of accretion (see S. Gezari 2021 for a recent review of TDEs).

If the star is completely disrupted, the rate at which the bound material falls onto the black hole scales as $t^{-5/3}$ at late

 Original content from this work may be used under the terms of the [Creative Commons Attribution 4.0 licence](#). Any further distribution of this work must maintain attribution to the author(s) and the title of the work, journal citation and DOI.

times (M. J. Rees 1988; E. S. Phinney 1989). For partial disruptions, the fallback rate can be steeper (J. Guillochon & E. Ramirez-Ruiz 2013; E. R. Coughlin & C. J. Nixon 2019; F. G. Goicovic et al. 2019; T. Ryu et al. 2020b), reaching $t^{-9/4}$ at late times (E. R. Coughlin & C. J. Nixon 2019). This material is expected to form an accretion disk that emits X-ray radiation (J. K. Cannizzo et al. 1990), as was indeed observed (see R. Saxton et al. 2021 for a recent review of X-ray TDEs).

In the past decade, however, another class of TDEs has been found that, surprisingly, emits mostly in the optical and ultraviolet (S. Gezari et al. 2012; I. Arcavi et al. 2014; see S. van Velzen et al. 2020 for a recent review of optical-ultraviolet TDEs). This class of events exhibits roughly constant blackbody temperatures of a few $\times 10^4$ K (1–2 orders of magnitude smaller than expected from an accretion disk), blackbody radii of $\sim 10^{15}$ cm (2 orders of magnitude larger than the tidal disruption radius of a Sun-like star), total released energies of 10^{50} – 10^{51} erg (2–3 orders of magnitude lower than the expected energy released by the accretion of a solar mass of material at 10% efficiency; the so-called “missing energy problem”), and broad H and/or He emission features in their spectra (which were not predicted). Yet these transients occur in otherwise quiescent and non-star-forming galaxies, disfavoring extreme active galactic nucleus (AGN) variability and massive-star explosions as their origin. More strikingly, their rates drop dramatically (faster than the SMBH mass function) in galaxies hosting SMBHs with masses above $10^8 M_{\odot}$ (S. van Velzen 2018; Y. Yao et al. 2023), providing “smoking gun” evidence that these transients “know” about the SMBH event horizon. Thus, both analytical models and numerical simulations of TDEs have tried to reconcile the discrepancies between TDE theory and observations of optical-ultraviolet TDEs either by invoking material to reprocess the emission from an accretion disk (J. Guillochon et al. 2014; N. Roth et al. 2016; L. Dai et al. 2018; B. Mockler et al. 2019) or by associating the emission with the collision of stellar debris streams before the accretion disk is formed (T. Piran et al. 2015).

Adding to the puzzle, a few optical transients, all in galaxy centers, were recently suggested to be repeating TDEs. ASASSN-14ko (A. V. Payne et al. 2021) shows tens of flares with a period of approximately 114 days, which slowly decreases with time (this period decrease has been explained using energy imparted to the surviving stellar core in the form of rotation, which should stop once the core is roughly “tidally locked” at pericenter; A. Bandopadhyay et al. 2024). The optical spectra of ASASSN-14ko are not typical of optical-ultraviolet TDEs but are more similar to those of AGN. An alternative explanation has been proposed, in which ASASSN-14ko is due to a star punching through an existing accretion disk around a black hole, with the period decrease due to hydrodynamical drag (I. Linial & E. Quataert 2024).

AT 2019aal (P. M. Veres et al. 2024) and AT 2021aeuk (J. Sun et al. 2025) show double flares within 3–4 yr but are both in previously known AGN and show spectra similar to AGN and Bowen fluorescence flares (BFFs; B. Trakhtenbrot et al. 2019). The nature of BFFs is not yet clear, but their occurrence in AGN (L. Makrygianni et al. 2023) suggests they could be related to accretion disk instabilities rather than TDEs.

AT 2018fyk (T. Wevers et al. 2019, 2023) was seen to rebrighten in the X-ray and ultraviolet wavelengths

approximately 1200 days after its first flare (T. Wevers et al. 2023). However, the first flare of AT 2018fyk was atypical of optical-ultraviolet TDEs, having a double-peak structure in its light curve and Fe lines in its spectra. This event has also been suggested as a possible single TDE around an SMBH binary (S. Wen et al. 2024).

AT 2020vdq (J. J. Somalwar et al. 2025b) showed two flares separated by 2.6 yr, discovered through a dedicated search for repeating TDEs, with the second flare showing spectra typical of optical-ultraviolet TDEs (J. J. Somalwar et al. 2025b). Unfortunately, there are no published optical spectra taken during the first flare. It has therefore not been determined whether the first flare of AT 2020vdq was due to an unrelated transient. Type Ia supernovae, for example, are ~ 50 times more common observationally than TDEs in galaxy centers (Y. Dgany et al. 2023), and one was indeed observed within 2 yr of the TDE AT 2021mhg at the same position (J. J. Somalwar et al. 2025b). In addition, for the first flare of AT 2020vdq to be a TDE, it would need to be one of the faintest and lowest-temperature TDEs ever observed (J. J. Somalwar et al. 2025b). Even if both flares of AT 2020vdq were indeed TDEs, it is not trivial to associate them with the disruption of the same star, given that the two flares differ substantially in their photometric properties and that their spectral similarity cannot be determined. In addition, the host galaxy of AT 2020vdq is a post-starburst galaxy. Such galaxies have been shown to exhibit an elevated TDE rate (I. Arcavi et al. 2014; K. D. French et al. 2016, 2020), which could produce two unrelated flares on the observed timescales at a nonnegligible probability (as we show in Section 5.2.2).

AT 2022dbl (I. Arcavi 2022; K. Z. Stanek 2022) is an otherwise “standard” optical-ultraviolet TDE with a nearly identical repetition 700 days after the first flare (Y. Yao et al. 2024). Both of the flares are very similar photometrically and nearly identical spectroscopically, such that J. T. Hinkle et al. (2024) and Z. Lin et al. (2024) claim (after ruling out an AGN origin) that both flares are due to the repeated disruption of the same star. However, the similarity between the flares could, in principle, be driven by the SMBH, with the two disruptions being of unrelated stars. In addition, the host of AT 2022dbl is a quiescent Balmer-strong galaxy. Such galaxies also show an elevated TDE rate. Albeit lower than the TDE rate enhancement seen in post-starburst galaxies (K. D. French et al. 2016, 2020), this specific galaxy was preselected as a potential TDE host due to its quiescent Balmer-strong properties (K. D. French & A. I. Zabludoff 2018). It remains to be shown how likely it is to observe two unrelated flares from such a galaxy on the observed timescales in order to securely determine the nature of AT 2022dbl.

Here, we present new observations and analysis of AT 2022dbl and a new analysis of its host galaxy, as well as of the host galaxy of AT 2020vdq. Our results securely establish AT 2022dbl as the first robust case of a repeating “normal” optical-ultraviolet TDE. We further discuss the far-reaching implications of this conclusion on the entire class of optical-ultraviolet TDEs.

2. Discovery and Classification

On 2022 February 17 (UT used throughout), we identified ZTF18aabdjx in the Zwicky Transient Facility (ZTF; E. C. Bellm et al. 2019) alert stream as a potential TDE after a significant brightening was detected on 2022 February 13 (MJD = 59623.37) using search criteria tailored to find TDEs

(Y. Dgany et al. 2023). The event is located at the center of the $z = 0.0284$ galaxy WISEA J122045.05+493304.7, which, as mentioned above, was preselected as a potential TDE host due to its quiescent Balmer-strong properties (K. D. French & A. I. Zabludoff 2018), similar to those of other TDE host galaxies (I. Arcavi et al. 2014; K. D. French et al. 2016, 2020). We consider the two r -band detections at the same position by ZTF in 2018, which were reported to the Transient Name Server (TNS) and received the name AT2018mac, as due to image-subtraction artifacts. AT2022dbl was spectroscopically classified on 2022 February 21 as a member of the optical-ultraviolet TDE class (I. Arcavi et al. 2022). On 2022 February 22, the event was reported (K. Z. Stanek 2022) to the TNS following an independent detection by the All-Sky Automated Survey for Supernovae (B. J. Shappee et al. 2014), and it received the name AT2022dbl. A second flare of AT2022dbl was reported to the TNS (Y. Yao et al. 2024) on 2024 February 6.

3. Observations

3.1. Optical, Ultraviolet, and Mid-infrared Photometry

We obtained optical photometry in the $BVgri$ bands starting on MJD 59632 with our own program on the Las Cumbres Observatory global network of 1 m telescopes (T. M. Brown et al. 2013). We obtained reference images from Las Cumbres Observatory on MJD 59951, approximately 1 yr after the first flare was detected. After the detection of the second flare, we restarted the follow-up of the event on MJD 60473. We used the LCOGTSNPIPE image-subtraction pipeline (S. Valenti et al. 2016) in order to remove host-galaxy emission. The pipeline generates the point-spread function (PSF) for each image and uses an implementation of the High Order Transform of PSF AND Template Subtraction (A. Becker 2015) to perform image subtraction and then PSF photometry at the source position. B - and V -band photometry were calibrated to the Vega system using the American Association of Variable Star Observers Photometric All-Sky Survey catalog (A. A. Henden et al. 2016), while gri -band photometry was calibrated to the AB system using the Sloan Digital Sky Survey (SDSS) Data Release (DR) 14 catalog (B. Abolfathi et al. 2018).

We further retrieved PSF-fit photometry of reference-subtracted images from the ZTF forced photometry service between MJD 58194 and 60422 and from the Asteroid Terrestrial-impact Last Alert System (ATLAS; J. L. Tonry et al. 2018) forced photometry service between MJD 57232 and 60438 at the position of AT2022dbl. The last pre-discovery nondetection upper limits at the position of AT2022dbl were obtained by ZTF approximately 100 days before the first detection with 3σ nondetection limits of 20.8 mag in the r band and 20.7 mag in the g band.

Target-of-opportunity observations (PIs: Arcavi, Makrygianni, Jiang, Hammerstein, and Lin) were obtained with the Neil Gehrels Swift Observatory (hereafter Swift; N. Gehrels et al. 2004) Optical/Ultraviolet Telescope (UVOT; P. W. A. Roming et al. 2005). In total, 81 epochs of imaging were obtained, spanning from MJD 59637 to 60470, in all six UVOT filters (UVW2, UVM2, UVW1, U , B , and V). We extracted photometry from the UVOT images using the HEASoft software package (Nasa High Energy Astrophysics Science Archive Research Center Heasarc 2014) and the standard analysis task `uvotsource`. We performed aperture

photometry using a $5''$ aperture for the source and a $25''$ aperture for the background. We subtracted the host fluxes obtained using observations from 2023 March 9, which is during the quiescent phase between the two flares, from all other epochs.

The location of AT2022dbl was observed by the Transiting Exoplanet Survey Satellite (TESS; G. R. Ricker et al. 2015) in sectors 22, 48, 49, 75, and 76. Sector 22 in Cycle 2 covers the period from MJD 58897 to 58926, i.e., 2 yr before the first flare. Sectors 48 and 49 in Cycle 4 cover MJD 59607 to 59664, which coincides with the first flare. Sectors 75 and 76 in Cycle 6 cover MJD 60339 to 60395, which coincides with the second flare. The position of AT2022dbl in sector 75 is too close to the edge of the imaging array to obtain valid flux calibration; therefore, data from this sector were not used. We processed the TESS data using image subtraction and forced PSF photometry (M. M. Fausnaugh et al. 2021). We used a customized version of the ISIS pipeline (C. Alard & R. H. Lupton 1998) to perform image subtraction for the science images within each sector with reference images built from the 20 lowest background images in the first 7 days of the sector (as cross-sector subtractions are not possible). We used the quiescent phase at the start of sector 48 (before the first flare) to determine the zero level of the flux from the mean of the photometry and the typical flux errors from the scatter of the photometry during this epoch. We treated any subsequent flux level that is below 3 times this scatter as a nondetection. Since the first 7 days of sector 49 included TDE light, subtracting their photometry from the photometry of the rest of the sector causes an underestimation of the TDE luminosity. Unfortunately, we found the background levels at the end and start of each sector to be too high to extract photometry from those epochs. This leads to gaps in the TESS light curve and prohibits scaling any oversubtracted sector to the sector before it. We therefore were unable to fully calibrate the TESS photometry, and we do not use it for any modeling purposes. We present it here only for completeness.

We queried the NASA/IPAC Infrared Science Archive²³ for mid-infrared (MIR) detections within $5''$ of the ZTF-determined position of AT2022dbl. This position has been visited approximately twice a year by NEOWISE-R (A. Mainzer et al. 2011, 2014) since MJD 56803. We rebinned the measurements available for each visit (using a weighted mean) into one representative measurement per year per band. We estimated the host-galaxy MIR flux and its uncertainty as the average and variance (respectively) of all pre-TDE epochs, and then we subtracted it from all observations. We found no significant MIR activity out to ~ 2 yr after the first peak at the 3σ level.

All of our photometry is presented in Figure 1 and Table 1. The Las Cumbres B - and V -band photometry is presented in the Vega system, and all other photometry is in the AB system.

3.2. Optical Spectroscopy

We obtained optical spectroscopy of AT2022dbl using our program on the FLOYDS spectrograph (D. J. Sand et al. 2011) mounted on the robotic 2 m Faulkes Telescope North at Haleakalā, Hawaii, which is part of the Las Cumbres Observatory network. FLOYDS covers the 3500–10000 Å range in a single exposure by capturing two spectral orders

²³ <https://irsa.ipac.caltech.edu/frontpage/>

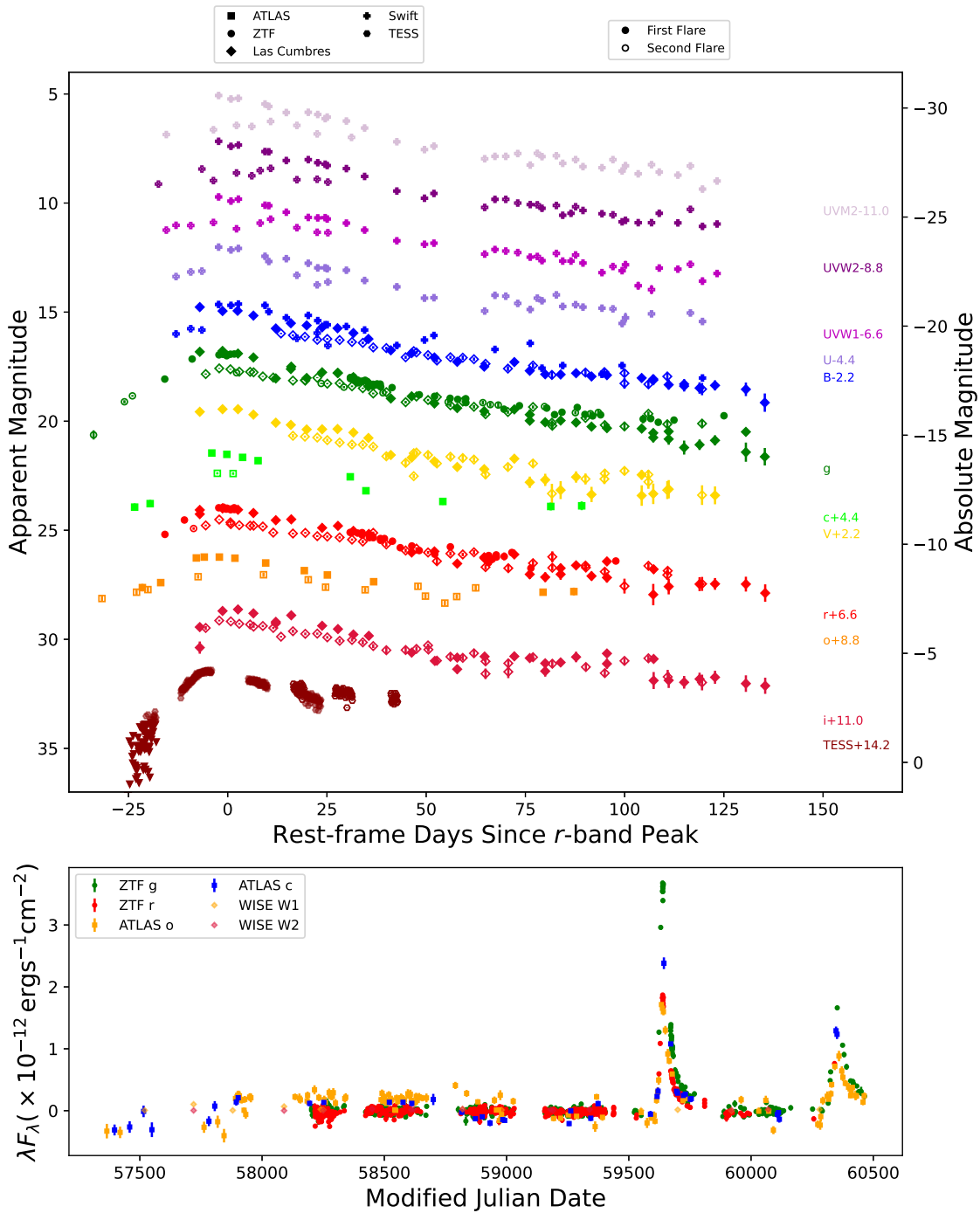


Figure 1. Optical and ultraviolet host-subtracted light curves of AT 2022dbl normalized to each peak time and shifted in magnitude for clarity (both flares are shifted by the same amount per band; top). Both flares are very similar to each other in the optical bands and show some differences in the ultraviolet. No earlier flares were detected in the ~ 1500 days preceding the first flare (bottom). Error bars denote 1σ uncertainties, and triangles denote 3σ nondetection upper limits.

simultaneously, with a spectral resolution of $R \sim 500$ using a slit width of $2''$. The spectra were reduced with a custom data reduction pipeline²⁴ built with the IRAF-free PYTHON-based ASPIRED toolkit (M. C. Lam & R. J. Smith 2022; M. C. Lam et al. 2023). Standard data reduction procedures were applied to trace and then optimally extract the spectral information (K. Horne 1986). Wavelength calibration was performed using the built-in calibrator powered by RASCAL (J. Veitch-Michaelis & M. C. Lam 2020, 2021). Standard stars

from the same night were used for flux calibration when available; otherwise, standard stars observed closest in time to the science observations were used. Finally, atmospheric extinction and telluric absorption were removed. We obtained five additional optical spectra with the Intermediate Dispersion Spectrograph mounted on the 2.54 m Isaac Newton Telescope at La Palma, Spain, under the Gravitational-wave Optical Transient Observer (D. Steeghs et al. 2022) Fast Analysis and Spectroscopy of Transients program. The spectra were obtained using the RED+2 detector with the R150V grism with a resolution of $R \sim 600$ at 4500 Å. The data were reduced

²⁴ https://github.com/cylanmarco/FLOYDS_pipeline

Table 1
AT 2022dbl Photometry

MJD	Filter	Magnitude	Error	Source
59532.52	<i>g</i>	>20.70	...	ZTF
59550.47	<i>g</i>	>20.91	...	ZTF
59623.33	<i>g</i>	18.13	0.03	ZTF
59630.42	<i>g</i>	17.21	0.01	ZTF
59637.37	<i>g</i>	17.02	0.01	ZTF
59639.32	<i>g</i>	17.02	0.01	ZTF
59671.43	<i>g</i>	18.06	0.02	ZTF
59674.38	<i>g</i>	18.23	0.03	ZTF
59729.90	<i>r</i>	19.93	0.13	Las Cumbres
59733.90	<i>r</i>	20.51	0.19	Las Cumbres
59737.90	<i>r</i>	20.01	0.18	Las Cumbres
59750.00	<i>r</i>	20.57	0.18	Las Cumbres
59632.40	<i>i</i>	17.26	0.16	Las Cumbres
59642.30	<i>i</i>	17.86	0.14	Las Cumbres

Note. Upper limits denote 3σ nondetections.

(This table is available in its entirety in machine-readable form in the [online article](#).)

using a custom recipe for the PyPeIt spectral reduction pipeline (J. X. Prochaska et al. 2020). We obtained two additional optical spectra with the Alhambra Faint Object Spectrograph and Camera mounted on the Nordic Optical Telescope at La Palma, Spain, using the Gr4 grism and $1''$ slit (resulting in a spectral resolution of $R \sim 300$). These spectra were reduced using the PyNOT-spex pipeline. We present all spectra in Figure 2.

3.3. X-Ray Observations

X-ray observations with the X-Ray Telescope (XRT; D. N. Burrows et al. 2005) on Swift were obtained simultaneously with the UVOT observations. Using XIMAGE to process the Swift/XRT images, we found no significant X-ray detection at the position of AT 2022dbl. We then used XIMAGE to calculate the corresponding flux upper limits for each of the XRT epochs, using a circular aperture with a radius of $\sim 47''$ centered on the (optical) position of AT 2022dbl (we verified that no neighboring X-ray sources are detected within that aperture). Using $n_{\text{H}} = 1.94 \times 10^{20} \text{ cm}^{-2}$, we derive 3σ upper limits for the absorbed flux across all epochs in the range of $1.1 \times 10^{-13} \text{ erg cm}^{-2} \text{ s}^{-1}$ to $1.2 \times 10^{-12} \text{ erg cm}^{-2} \text{ s}^{-1}$, which corresponds to $L(0.2\text{--}10 \text{ keV}) < 2.0 \times 10^{41} \text{ erg s}^{-1}$. Combining all epochs of the Swift XRT data (~ 31 ks exposure), we still do not detect any significant X-ray emission and set a 3σ upper limit of $1.4 \times 10^{-14} \text{ erg cm}^{-2} \text{ s}^{-1}$, which corresponds to $L(0.2\text{--}10 \text{ keV}) < 2.6 \times 10^{40} \text{ erg s}^{-1}$.

3.4. Radio Observations

We observed the position of AT 2022dbl using the Karl G. Jansky Very Large Array (VLA) under programs 21A-184 and 22A-163 (PI: Horesh). Our VLA observations were carried out on MJDs 59636, 59800, and 60152 using the *S*, *C*, *X*, and *Ku* bands. The VLA was in the BnA→A configuration during the first observation, the D configuration during the second observation, and the A configuration during the third observation. Automatic flagging and calibration of the data were conducted with the VLA calibration pipeline. We used 3C 286 as a primary flux calibrator and J1219+4829 as a

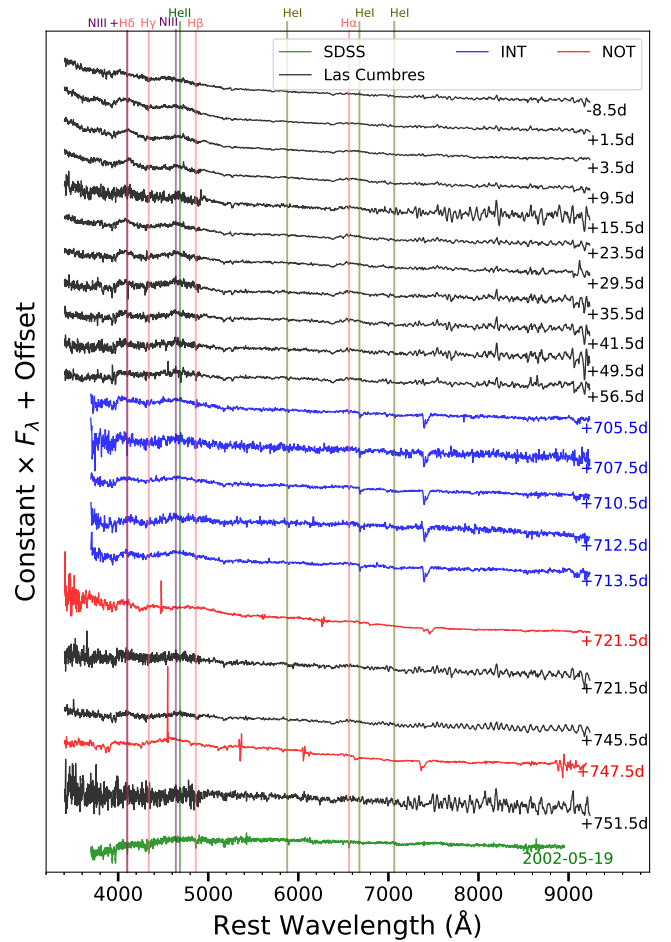


Figure 2. Our full spectral series of AT 2022dbl together with the host-galaxy spectrum from SDSS. Lines that characterize various subtypes of optical-ultraviolet TDEs are marked. Phases are noted in days relative to the peak luminosity of the first flare.

phase calibrator. Images of the field of AT 2022dbl were produced with the CASA tCLEAN task in an interactive mode. When a source was detected at the phase center, we fitted it with the CASA task IMFIT, and the image rms was calculated using the CASA task IMSTAT. We estimate the error of the peak flux density to be a quadratic sum of the error produced by the CASA task IMFIT and a 10% calibration error. We detected radio emission consistent with the position of AT 2022dbl, which we present in Figure 3 and Table 2.

We also carried out multiple observations in the 15.5 GHz band with the Arcminute Micro-Kelvin Imager—Large Array (AMI-LA; J. T. L. Zwart et al. 2008; J. Hickish et al. 2018) from shortly after optical discovery until more than 700 days later. Initial flagging and reduction were conducted using `reduce_dc`, a customized AMI-LA data reduction software package (Y. C. Perrott et al. 2013). We use the same primary flux phase calibrators as above. Images of the field of AT 2022dbl were produced with the CASA CLEAN task in an interactive mode, and the image rms was calculated using the CASA task IMSTAT. These observations were less sensitive than our VLA observations and resulted in null detections. Our 3σ upper limits for the emission from AT 2022dbl are provided in Table 2.

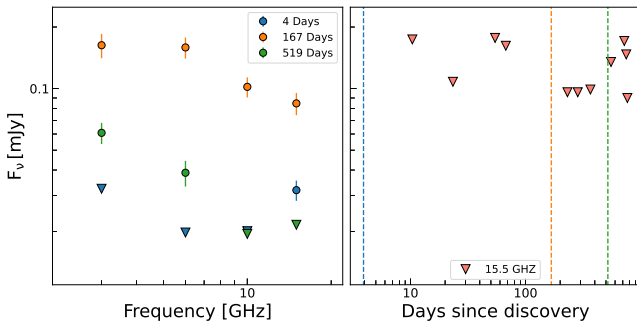


Figure 3. Radio spectra at three different epochs (left; denoted in days since optical discovery) and the 15.5 GHz light curve (right) of AT 2022dbl, with dashed vertical lines marking the spectral epochs. Error bars denote 1σ uncertainties, and triangles mark 3σ nondetection upper limits.

4. Analysis

4.1. Optical and Ultraviolet Photometric Analysis

4.1.1. Peak Time, Blackbody, and Decline Rate

We fit a second-degree polynomial around the r -band peak of each flare to determine a peak luminosity time of MJD 59639.67 ± 1.16 for the first flare and MJD 60350.92 ± 1.09 for the second flare. This gives a time difference of 711.25 ± 1.59 days between peaks.

We fit a blackbody to the ZTF (g and r), ATLAS (c and o), Las Cumbres (g , r , i , B , and V), and Swift ultraviolet photometry for each epoch in which we have Swift data (linearly interpolating neighboring optical epochs) using SUPERBOL (M. Nicholl 2018). We exclude epochs without Swift data given the systematic uncertainties introduced when fitting hot blackbodies without ultraviolet observations (I. Arcavi 2022).²⁵ We then calculate the bolometric luminosity by integrating each observed spectral energy distribution, with the missing flux outside the observed bands taken under the assumption of a blackbody with the best-fit parameters. Our results are presented in Figure 4 and Table 3. The best-fit temperature and resulting bolometric luminosities of both flares, as well as their evolution in time, are typical of TDEs, while the blackbody radii are on the low end of the known sample. The second flare peak bolometric luminosity is approximately 4 times fainter than that of the first flare. The bolometric peak luminosity of the first (second) flare is $\gtrsim 500$ ($\gtrsim 10$) times brighter than the per-epoch X-ray nondetection limits and $\gtrsim 3700$ ($\gtrsim 80$) times brighter than the stacked X-ray nondetection limit. These values are consistent with blackbody-to-X-ray luminosity ratios observed in other TDEs (M. Guolo et al. 2024).

We fit the postpeak bolometric light curve (i.e., the luminosity L versus time t) of each flare with a power law of the form $L = L_0[(t - t_0)/\tau]^{-\alpha}$ and an exponential decay of the form $L = L_0 e^{-t/\tau}$. For the first flare, we perform the power-law fit twice, once with t_0 as a free parameter and once with t_0 fixed to 33.7 days before peak (the fallback time of the most bound debris obtained from fitting the light curve with a reprocessing emission TDE model; see below). L_0 and τ are strongly degenerate and hence are not constrained individually. Here we focus on the power law α , which has the most value in constraining physical scenarios. Our best-fit results

²⁵ Unfortunately, before peak, there are not enough data, even in the optical alone, to constrain the blackbody parameters.

Table 2
AT 2022dbl Radio Observations

MJD	Frequency (GHz)	F_ν (mJy)	Error (mJy)	Source
59627	3	≤ 0.033	0.011	VLA:BnA→A
59627	6	≤ 0.02	0.006	VLA:BnA→A
59627	10	≤ 0.02	0.006	VLA:BnA→A
59627	15	0.032 ± 0.004	0.006	VLA:BnA→A
59633	15.5	≤ 0.17	0.058	AMI-LA
59646	15.5	≤ 0.11	0.036	AMI-LA
69677	15.5	≤ 0.18	0.059	AMI-LA
59690	15.5	≤ 0.16	0.054	AMI-LA
59790	3	0.16 ± 0.02	0.020	VLA:D
59790	6	0.16 ± 0.02	0.015	VLA:D
59790	10	0.10 ± 0.01	0.009	VLA:D
59790	15	0.085 ± 0.010	0.015	VLA:D
59854	15.5	≤ 0.10	0.032	AMI-LA
59907	15.5	≤ 0.10	0.032	AMI-LA
59989	15.5	≤ 0.10	0.033	AMI-LA
60142	3	0.061 ± 0.007	0.009	VLA:A
60142	6	0.039 ± 0.006	0.006	VLA:A
60142	10	≤ 0.02	0.006	VLA:A
60142	15	≤ 0.021	0.007	VLA:A
60176	15.5	≤ 0.14	0.045	AMI-LA
60344	15.5	≤ 0.17	0.057	AMI-LA
60373	15.5	≤ 0.15	0.049	AMI-LA
60390	15.5	≤ 0.09	0.030	AMI-LA

Note. Upper limits denote 3σ nondetections.

are presented in Figure 4 and Table 4. The data are better described by a power law than an exponential, with the first flare decline preferring $\alpha = 2.6$ – 2.7 , steeper than the canonical $\alpha = 5/3$ power law for the mass fallback rate of a full disruption (M. J. Rees 1988; E. S. Phinney 1989). Such a steep decline has been seen in a few optical-ultraviolet TDEs (e.g., M. Nicholl et al. 2020; P. Charalampopoulos et al. 2023) and is close to the expected values for partial disruptions (e.g., E. R. Coughlin & C. J. Nixon 2019). The decline rate of the second flare is more difficult to constrain given the available data. For fixed t_0 at 44.65 days before peak (estimated in the same way as for the first flare), the fit is consistent with a canonical $\alpha = 5/3$ decline, but it is not possible to determine if this is part of a broad peak that later settled to a steeper decline. We were not able to obtain any constraining fits using a free t_0 for the second flare.

4.1.2. Analytical TDE Models

We use the Modular Open Source Fitter for Transients (MOSFiT; J. Guillochon et al. 2018) to fit the multiband light curves of AT 2022dbl with a TDE emission model (B. Mockler et al. 2019) that assumes a mass fallback rate derived from simulated disruptions (J. Guillochon et al. 2014) of polytropic stars by a black hole of $10^6 M_\odot$. This model then uses scaling relations and interpolations for a range of black hole masses, star masses, and encounter parameters. The free parameters of the model are the mass of the black hole, M_{BH} , and star, m_* ; the scaled impact parameter b (which is defined in such way that $b = 0$ corresponds to no disruption, while $b \geq 1$ corresponds to a full disruption); the efficiency ϵ of converting accreted mass to energy; the unitless normalization and power-law index, $R_{\text{ph},0}$ and l_{ph} , respectively, connecting the radius to the instantaneous luminosity; the viscous delay time T_ν (the timescale for matter

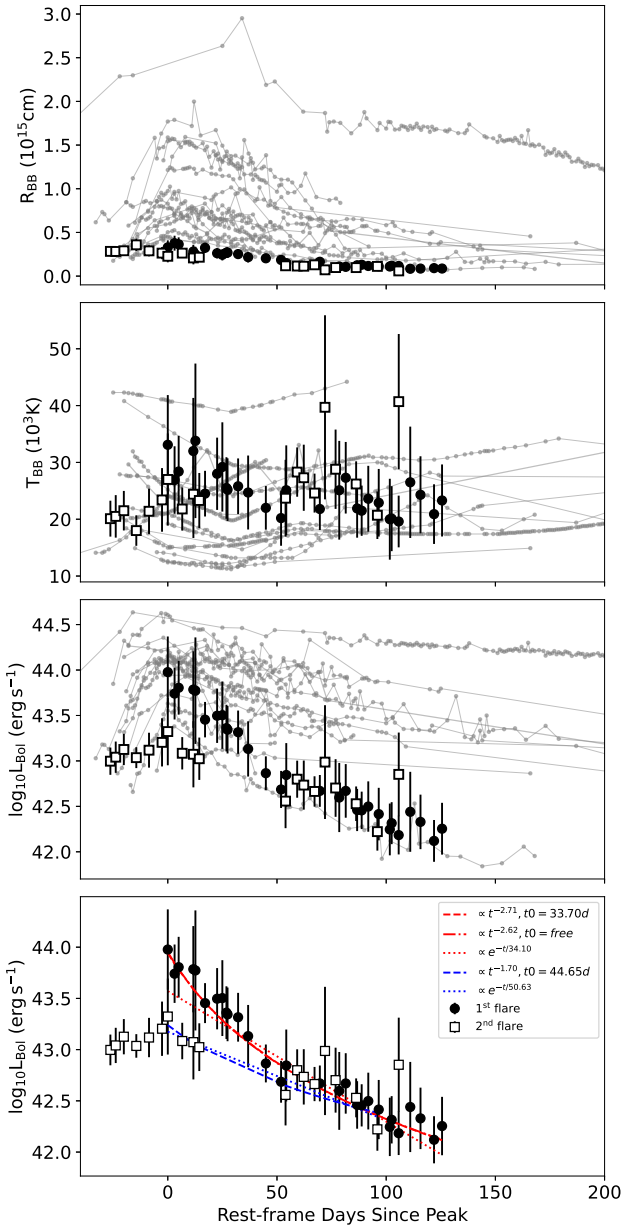


Figure 4. AT2022dbl best-fit blackbody radius, temperature, and resulting bolometric luminosity (top to bottom panels; black filled and open markers for the first and second flares, respectively). The temperature and luminosity are within the range of a comparison sample of TDEs (S. van Velzen et al. 2020; gray), while the radius is on the lower end of the sample. Fits to the postpeak decline of the bolometric luminosity are also shown (bottom panel). Error bars denote 1σ uncertainties and are shown only for AT2022dbl for clarity.

to circularize and/or move through the accretion disk), which acts approximately as a low-pass filter on the light curve; the time of first fallback, t_0 ; the extinction, proportional to the hydrogen column density n_H in the host galaxy; and a white-noise parameter, σ . We use the nested sampling method implemented through DYNESTY (J. S. Speagle 2020), as appropriate for complex posteriors in high-dimensional parameter spaces. We list the prior distributions for the parameters along with the posteriors in Table 5. The light-curve fits are presented in Figure 5, and the two-dimensional posterior distributions are presented in Figure 6. We find that the first (second) flare of AT2022dbl is best described by the disruption of an $m_* = 0.1034^{+0.0121}_{-0.0044} \pm 0.6600 M_\odot$

($m_* = 0.37^{+0.30}_{-0.18} \pm 0.66 M_\odot$) star by a black hole of mass $\log(M_{\text{BH}}/M_\odot) = 6.698^{+0.076}_{-0.087} \pm 0.200$ ($\log(M_{\text{BH}}/M_\odot) = 6.63^{+0.11}_{-0.10} \pm 0.20$, statistical and systematic uncertainties (B. Mockler et al. 2019) reported). There is a strong degeneracy between the stellar mass and efficiency parameter in this model (B. Mockler & E. Ramirez-Ruiz 2021). The derived parameters are consistent between both flares, and the black hole mass estimate is also consistent with the value found from the galaxy scaling relation described below. The best scaled impact parameter of the first (second) flare is $b = 0.984^{+0.054}_{-0.081} \pm 0.350$ ($b = 1.157^{+0.096}_{-0.148} \pm 0.350$). While the scaled impact parameter of the second flare is more consistent with a full disruption, the posterior for the first flare spreads both below and above 1 (Figure 6), meaning that it is consistent with both a full and partial disruption. The difference in the photospheric radius normalization factor $R_{\text{ph},0}$ between flares is likely due in large part to the difference in bolometric luminosities and does not result in large differences in the actual photospheric radius determined by MOSFiT, which varies by a factor of $\lesssim 2$ between flares.

To estimate the black hole and stellar masses based on the stream collision scenario (T. Piran et al. 2015; Y.-F. Jiang et al. 2016), we use the TDEMass package (T. Ryu et al. 2020a). This package fits the mass of the black hole and the disrupted star to the peak bolometric luminosity and the temperature at this time. For the first (second) flare, we find a stellar mass of $m_* = 0.87^{+0.39}_{-0.46}$ ($m_* = 0.40^{+0.34}_{-0.30}$) and a black hole mass of $\log(M_{\text{BH}}/M_\odot) = 6.00^{+0.69}_{-0.36}$ ($\log(M_{\text{h}}/M_\odot) = 5.54^{+1.61}_{-0.26}$). Again, both flares are consistent with each other, and the black hole mass is consistent with the one derived from the galaxy scaling relation described below.

4.1.3. Numerical TDE Model

As illustrative cases, we repeat the hydrodynamical simulations of A. Bandopadhyay et al. (2024) for two scenarios. The first is the repeated partial disruption of a $3 M_\odot$ evolved star (we do not consider more massive stars given the stellar population age of the host galaxy; see below) by a $10^6 M_\odot$ black hole, for which the binding energy of the star to the black hole was chosen such that the orbital period of the star was ~ 700 days and its pericenter radius was equal to R_t . The second simulation is of the disruption of a $1 M_\odot$ star at the zero-age main sequence by a $10^6 M_\odot$ black hole with a pericenter of $\sim R_t/1.4$.

We use the smoothed particle hydrodynamics code PHANTOM (D. J. Price et al. 2018) to simulate the repeated partial disruption of two stars, a $3 M_\odot$ evolved star and a $1 M_\odot$ zero-age main-sequence star, by a $10^6 M_\odot$ black hole. Using the stellar evolution code MESA (B. Paxton et al. 2011), we evolve the stars along the main sequence. The density profiles of the stars are then mapped onto a three-dimensional particle distribution in PHANTOM and relaxed for \sim five sound-crossing times across the stellar radius (E. C. A. Golightly et al. 2019). We use a resolution of 10^6 particles to model the stars. The center of mass of the star is placed on a bound orbit around the black hole with an orbital period of 700 days and a pericenter distance of $R_p \sim R_t$ for the $3 M_\odot$ star and $R_p \sim R_t/1.4$ for the $1 M_\odot$ star. The resulting mass fallback rates from the simulations are shown in Figure 7. Both scenarios are consistent with the bolometric light curves of AT2022dbl, assuming the bolometric light traces the mass fallback rate. More details can be found in A. Bandopadhyay et al. (2024).

Table 3
AT 2022dbl Best-fit Blackbody Parameters

Phase (days)	Temperature (10^4 K)	Error (10^4 K)	Radius (10^{14} cm)	Error (10^{14} cm)	Luminosity (10^{43} erg s $^{-1}$)	Error (10^{43} erg s $^{-1}$)
0.0	3.31	0.88	3.29	0.80	9.48	8.56
3.112	2.69	0.60	3.77	0.85	5.51	3.61
4.979	2.84	0.63	3.64	0.80	6.38	4.35
11.688	3.20	0.94	2.81	0.77	6.10	5.91
12.651	3.38	1.36	2.47	0.89	5.93	8.00
17.056	2.45	0.40	3.24	0.57	2.84	1.28
22.588	2.80	0.64	2.62	0.59	3.14	2.16
24.981	2.92	0.79	2.44	0.65	3.18	2.71
26.848	2.55	0.54	2.69	0.59	2.30	1.36
27.363	2.52	0.55	2.69	0.62	2.21	1.33
32.196	2.58	0.50	2.52	0.50	2.07	1.13
36.785	2.47	0.65	2.17	0.61	1.36	9.49
44.905	2.20	0.38	2.04	0.42	0.73	0.31
51.867	2.02	0.49	1.85	0.53	0.49	0.23
54.249	2.51	0.79	1.48	0.49	0.70	0.57
69.623	2.18	0.37	1.64	0.32	0.47	0.19
78.51	2.51	0.87	1.10	0.40	0.40	0.35
81.476	2.73	0.63	1.06	0.25	0.47	0.32
86.698	2.19	0.52	1.24	0.34	0.29	0.15
88.779	2.15	0.44	1.30	0.32	0.29	0.14
91.803	2.36	0.58	1.16	0.32	0.32	0.20
96.587	2.29	0.60	1.13	0.33	0.26	0.17
101.663	2.00	0.71	1.10	0.48	0.18	0.12
102.509	2.01	0.57	1.19	0.41	0.21	0.11
105.718	1.96	0.46	1.16	0.33	0.153	0.075
111.017	2.65	0.98	0.84	0.32	0.28	0.28
115.714	2.43	0.68	0.86	0.26	0.21	0.15
121.908	2.09	0.53	0.91	0.28	0.132	0.070
125.583	2.33	0.63	0.87	0.26	0.18	0.12
677.762	2.01	0.32	2.83	0.55	0.99	0.34
680.212	2.05	0.37	2.82	0.62	1.10	0.43
683.917	2.15	0.35	2.90	0.56	1.34	0.53
689.634	1.80	0.27	3.58	0.70	1.09	0.29
695.449	2.14	0.40	2.89	0.63	1.31	0.58
701.41	2.34	0.56	2.63	0.69	1.60	0.98
704.045	2.70	0.81	2.27	0.69	2.10	1.80
710.657	2.18	0.38	2.63	0.54	1.21	0.50
715.772	2.44	0.77	2.08	0.74	1.18	0.99
718.466	2.33	0.48	2.16	0.51	1.06	0.57
757.974	2.37	0.68	1.18	0.37	0.36	0.25
763.292	2.83	0.43	1.15	0.18	0.63	0.30
766.307	2.73	0.58	1.13	0.25	0.54	0.34
771.237	2.46	0.34	1.29	0.20	0.46	0.18
776.031	3.97	1.62	0.72	0.25	0.97	1.40
780.883	2.88	0.70	0.98	0.24	0.50	0.37
790.286	2.62	0.40	0.97	0.16	0.34	0.15
800.01	2.07	0.42	1.11	0.28	0.167	0.080

Note. Phase is given in days relative to the first bolometric peak.

In the first simulation, nearly identical mass fallback rates are produced for both flares (and predicted for a third flare; top panel of Figure 7). In the second simulation, the first encounter produces a rapidly declining mass fallback rate, while the second encounter produces a slightly lower mass fallback peak and subsequently slower decay (bottom panel of Figure 7). Both scenarios are consistent with the shape of the bolometric light curve of each flare (Figure 7), though the similarity in the spectral features of the flares (see below) is hard to explain if the two disruptions are significantly different from each other.

These simulations are not fits to the data but are presented as illustrative cases that explore the effect of varying the stellar

structure and the pericenter distance on the mass fallback rates from a star on a bound 700 day orbit around a $10^6 M_{\odot}$ black hole. They are shown with the data only to compare global behavior (such as timescales and decline rates) under the assumption that the fallback of stellar debris onto the black hole is the primary driver of TDE emission. Fitting the observed light curves with the simulated fallback rates would require an exhaustive set of numerical simulations that explores not only the effect of varying stellar structure but also other parameters such as the SMBH mass, orbital eccentricity, and pericenter distance, which is beyond the scope of this work. In addition, it would require a more precise

Table 4
AT 2022dbl Bolometric Decline Best-fit Parameters

Model	Parameters
Flare 1	
Power law (fixed $t_0 = -33.70$)	$\alpha = -2.71 \pm 0.10$ τ unconstrained L_0 unconstrained
Power law (free t_0)	$\alpha = -2.62 \pm 0.45$ τ unconstrained $t_0 = -34.51 \pm 11.82$ L_0 unconstrained
Exponential	$\tau = 34.10 \pm 2.44$ $L_0 = (3.72 \pm 0.56) \times 10^{43}$
Flare 2	
Power law (fixed $t_0 = -44.65$)	$\alpha = -1.70 \pm 0.25$ τ unconstrained L_0 unconstrained
Exponential	$\tau = 50.63 \pm 6.02$ $L_0 = (1.49 \pm 0.22) \times 10^{43}$

Note. τ and t_0 are given in days and L_0 in erg s^{-1} .

connection between the mass fallback rate and the emission, which is an open problem in TDE physics.

4.2. Spectroscopic Analysis

We identify three main broad emission features in the spectra of AT 2022dbl (Figure 2). The first, around 4100 Å, we attribute to N III $\lambda\lambda 4097, 4103$, possibly from the Bowen fluorescence mechanism (I. S. Bowen 1928; H. Netzer et al. 1985), as seen in other optical-ultraviolet TDEs (N. Blagorodnova et al. 2019; G. Leloudas et al. 2019). As argued previously (G. Leloudas et al. 2019), an association with H δ is less likely given a lack of (or very weak) H γ . Next, there is a very broad (and likely blended) feature from ~ 4300 Å to ~ 5000 Å that encompasses H β , He II $\lambda 4686$, and N III $\lambda 4640$. Last is the broad feature corresponding to H α . In addition, possible weak broad He I emission at 5876 Å can be seen after host and continuum subtraction (see below). These features classify AT 2022dbl as a ‘‘Bowen TDE’’ (S. van Velzen et al. 2020). We identify these features during both the first and the second flare, which exhibit nearly identical spectra.

In Figure 8, we compare the spectrum of AT 2022dbl near the peak of its first flare to the near-peak spectra of the Bowen TDEs ASASSN-14li (T. W. S. Holoiën et al. 2016), iPTF15af (N. Blagorodnova et al. 2019), iPTF16axa (T. Hung et al. 2017), iPTF16fnl (N. Blagorodnova et al. 2017; F. Onori et al. 2019), AT 2017eqx (M. Nicholl et al. 2019), AT 2018dyb (G. Leloudas et al. 2019), AT 2019dsg (G. Cannizzaro et al. 2021), and AT 2019qiz (M. Nicholl et al. 2020). While different events show different line profiles, the main features (namely, broad Balmer series, He II and N III emission lines) are common to all events.

We further analyze the spectra using a standard procedure (P. Charalampopoulos et al. 2022), which includes scaling the spectra to the *gri*-band photometry, correcting for Milky Way extinction, subtracting the host-galaxy spectrum from each TDE spectrum, and removing the continuum by fitting line-

free regions (3800–3900 Å, 4300–4400 Å, 5100–5500 Å, 6000–6300 Å, and 7100–7300 Å) with a fourth-degree polynomial. As the emission lines in the blue part of the spectrum are likely a blend of various species, we focus our spectroscopic analysis on the H α emission line. We use the LMFIT package to fit the line with a Gaussian profile and calculate the total integrated flux of the Gaussian and its full width at half-maximum (FWHM) for each spectrum. The uncertainties for the flux and line width are the 1σ uncertainty from the least-squares method used for the fitting.

We present the results in Figure 9 and compare them with a similar analysis performed by M. Nicholl et al. (2020) and P. Charalampopoulos et al. (2022, 2023) for the well-sampled Bowen TDEs ASASSN-14li (T. W. S. Holoiën et al. 2016), iPTF15af (N. Blagorodnova et al. 2019), iPTF16axa (T. Hung et al. 2017), iPTF16fnl (N. Blagorodnova et al. 2017; F. Onori et al. 2019), AT 2017eqx (M. Nicholl et al. 2019), AT 2018dyb (G. Leloudas et al. 2019), and AT 2019qiz (M. Nicholl et al. 2020), as well as the non-Bowen but rapidly declining TDE AT 2020wey (P. Charalampopoulos et al. 2023). AT 2022dbl has the weakest measured H α emission luminosity and lowest FWHM in the sample, perhaps representing a transition between H-rich and H-poor TDEs. The H α feature evolves similarly in both AT 2022dbl flares, compared to the spread in the comparison sample.

We find a time lag between the peak of the H α luminosity (determined using the brightest point) and that of the *g*-band light curve of $\sim 5.6 \pm 0.4$ days and $\sim 4.8 \pm 2.1$ days for the first and second flares, respectively. This timescale corresponds to a light travel distance of $(1.2\text{--}1.5) \times 10^{16}$ cm, which is 2 orders of magnitude larger than the blackbody radius of AT 2022dbl (where the continuum emission is formed). Similar results were found for other TDEs (P. Charalampopoulos et al. 2022).

4.3. Radio Analysis

The early radio emission observed with the VLA 4 days after optical discovery of the first flare revealed a faint 0.03 mJy source in the *Ku* band and null detections in the *S*, *C*, and *X* bands (left panel of Figure 3). The second spectrum obtained 167 days after optical discovery showed an optically thin emission at frequencies higher than 6 GHz and a possible transition to the optically thick regime around 3 GHz, with a peak flux of ~ 0.16 mJy. Finally, the last broadband spectrum, obtained 519 days after optical discovery, revealed optically thin emission at low frequencies (3–6 GHz) and null detections at higher frequencies, suggesting an optically thin spectrum at all GHz frequencies. The 15.5 GHz light curve obtained with the AMI-LA resulted in multiple null detections from 10 days to ~ 2 yr after optical discovery at a 3σ upper limit of 0.1–0.2 mJy (right panel of Figure 3).

Under an equipartition analysis (R. Barniol Duran et al. 2013), and using the lowest-frequency observed 167 days after optical discovery as an estimation of the peak flux density, we next estimate the physical parameters of the shock and its environment at that time. We assume that the spectral peak frequency is the synchrotron self-absorption frequency to estimate a radius for the emitting region of $\sim 2 \times 10^{16}$ cm and a minimal total energy of $\sim 3 \times 10^{47}$ erg, respectively. Here we used $\epsilon_e = \epsilon_B = 0.1$ (where ϵ_e and ϵ_B are the fractions of energy deposited in the relativistic electrons and the magnetic fields, respectively), an area filling factor of $f_A = 1$, a volume filling factor of $f_V = 4/3$, and an electron power-law index of $p = 2.5$.

Table 5
AT 2022dbl Best-fit MOSFiT Parameters and Priors Used

Parameter	Prior	Range	Best-fit Flare 1	Best-fit Flare 2	Systematic Error	Unit
M_{BH}	Log	$[10^5, 10^8]$	$6.698^{+0.076}_{-0.087}$	$6.629^{+0.110}_{-0.099}$	± 0.20	M_{\odot}
m_*	Kroupa	$[0.01, 100]$	$0.1034^{+0.0121}_{-0.0044}$	$0.37^{+0.30}_{-0.18}$	± 0.66	M_{\odot}
b	Flat	$[0, 2]$	$0.984^{+0.055}_{-0.081}$	$1.157^{+0.096}_{-0.148}$	± 0.35	...
ϵ	Log	$[0.005, 0.4]$	$-1.34^{+0.16}_{-0.18}$	$-2.13^{+0.20}_{-0.11}$	± 0.68	...
$R_{\text{ph},0}$	Log	$[10^{-4}, 10^4]$	$0.64^{+0.13}_{-0.12}$	$0.12^{+0.12}_{-0.17}$	± 0.40	...
l_{ph}	Flat	$[0, 4]$	$1.80^{+0.10}_{-0.10}$	$1.08^{+0.11}_{-0.10}$	± 0.20	...
T_{ν}	Log	$[10^{-3}, 10^3]$	$-1.43^{+1.02}_{-1.12}$	$-2.31^{+0.62}_{-0.45}$	± 0.10	days
t_0	Flat	$[-150, 0]$	$-11.94^{+1.87}_{-2.11}$	$-10.26^{+2.00}_{-2.50}$	± 15	days
$n_{\text{H,host}}$	Log	$[10^{19}, 10^{23}]$	$20.922^{+0.033}_{-0.039}$	$20.964^{+0.045}_{-0.053}$...	cm^{-2}
σ	Log	$[10^{-4}, 10^2]$	$-0.472^{+0.018}_{-0.017}$	$-0.683^{+0.027}_{-0.023}$

Note. Best-fit results are the median of each posterior distribution, and the uncertainties are the 16th and 84th percentiles. These error estimations do not include the systematic uncertainties estimated for MOSFiT (B. Mockler et al. 2019), shown in a separate column. ‘‘Log’’ in the Prior column denotes a log-uniform distribution and values that refer to the log of the parameter.

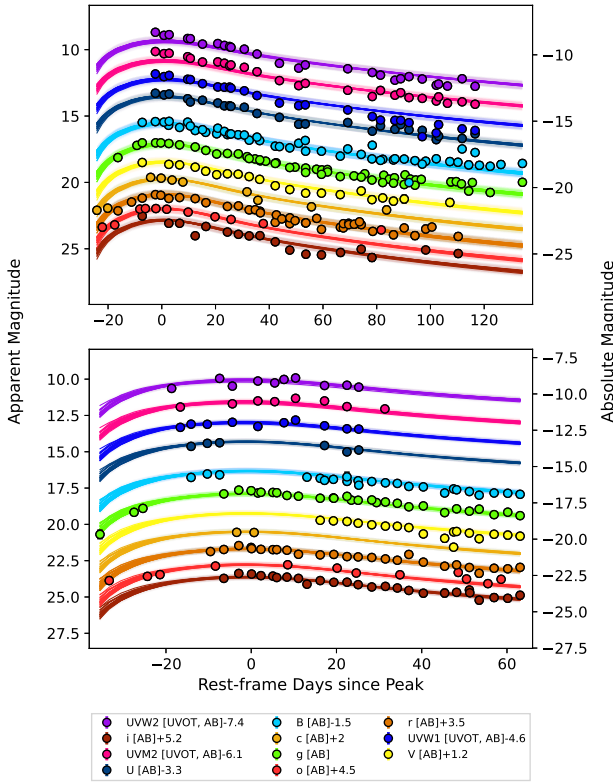


Figure 5. Reprocessed accretion emission MOSFiT model fits to the first (top) and second (bottom) flares of AT 2022dbl.

Assuming free expansion of the forward shock, we find a shock velocity of $\sim 13,000 \text{ km s}^{-1}$. We estimate the external density to be $\sim 70 \text{ cm}^{-3}$ by dividing the number of emitting electrons by $4V$, where V is the volume of the emitting region (a factor of 4 is needed to account for the shock jump conditions; R. Barniol Duran et al. 2013).

Since the transition to the optically thick regime is not observed, the analysis above should be taken with care as the uncertainties on the spectral peak are large. The spectrum obtained 167 days after discovery is the only one exhibiting the spectral peak; therefore, we do not use other spectra to estimate the physical parameters. However, the spectrum obtained 4 days after optical discovery shows optically thick emission at 15.5 GHz and therefore a spectral peak at higher

frequencies, and the spectrum at 519 days shows optically thin emission at 3 GHz and therefore a spectral peak at lower frequencies. This evolution of the spectral peak to lower frequencies is in agreement with the spectral evolution expected from a shock traveling in a declining density profile (R. A. Chevalier 1998).

Finally, while the 15.5 GHz light curve is not sensitive enough for the detection of the first flare, we are able to rule out a second, delayed, radio flare (as seen in some optical-ultraviolet TDEs; A. Horesh et al. 2021a, 2021b; Y. Cendes et al. 2022; I. Sfaradi et al. 2022, 2024) at luminosities of $(3\text{--}6) \times 10^{37} \text{ erg s}^{-1}$ during the first 2 yr after optical discovery.

4.4. Host Galaxy

The host galaxy of AT 2022dbl was classified as a quiescent Balmer-strong galaxy (K. D. French & A. I. Zabludoff 2018) based on its SDSS spectrum, having an SDSS $H\alpha$ equivalent width in emission of $-0.016 \pm 0.130 \text{ \AA}$ and an SDS Lick $H\delta_A$ index of $2.20 \pm 0.58 \text{ \AA}$. The MPA-JHU DR8 catalog lists a velocity dispersion of $\sigma = 60.0 \pm 5.1 \text{ km s}^{-1}$ for the galaxy. Using the $M_{\text{BH}}\text{--}\sigma$ relation (J. Kormendy & L. C. Ho 2013), we find a central black hole mass of $\log(M_{\text{BH}}/M_{\odot}) = 6.20 \pm 0.52$.

We retrieved *ugriz* photometry of the host galaxy from SDSS DR 15 (D. S. Aguado et al. 2019), *JHK* photometry from the Two Micron All Sky Survey (T. H. Jarrett et al. 2000), and W1, W2 photometry from the Wide-field Infrared Survey Explorer (through the AllWISE catalog; R. M. Cutri et al. 2021) using coadded images taken from 2010 May 25 to 2010 December 3 via the SDSS SkyServer and the NASA/IPAC Extragalactic Database. We also retrieved ultraviolet archival photometry from the Galaxy Evolution Explorer (M. Seibert et al. 2012). We fit the host-galaxy photometry using the PROSPECTOR (J. Leja et al. 2017) α model, similar to what was done in previous TDE host-galaxy studies (M. Nicholl et al. 2020; P. Ramsden et al. 2022). The free parameters in the model are the stellar mass, the stellar metallicity, a six-parameter star formation history, and three parameters that control the dust fraction and reprocessing. The observed host-galaxy spectral energy distribution and the best-fit PROSPECTOR models are shown in Figure 10. We find a stellar mass of $\log(M_*/M_{\odot}) = 10.36^{+0.02}_{-0.03}$, a subsolar metallicity of $\log(Z/Z_{\odot}) = -1.20^{+0.30}_{-0.28}$, and a low specific star formation rate of $\log(\text{sSFR}) = -12.56^{+0.41}_{-0.66}$ within the past

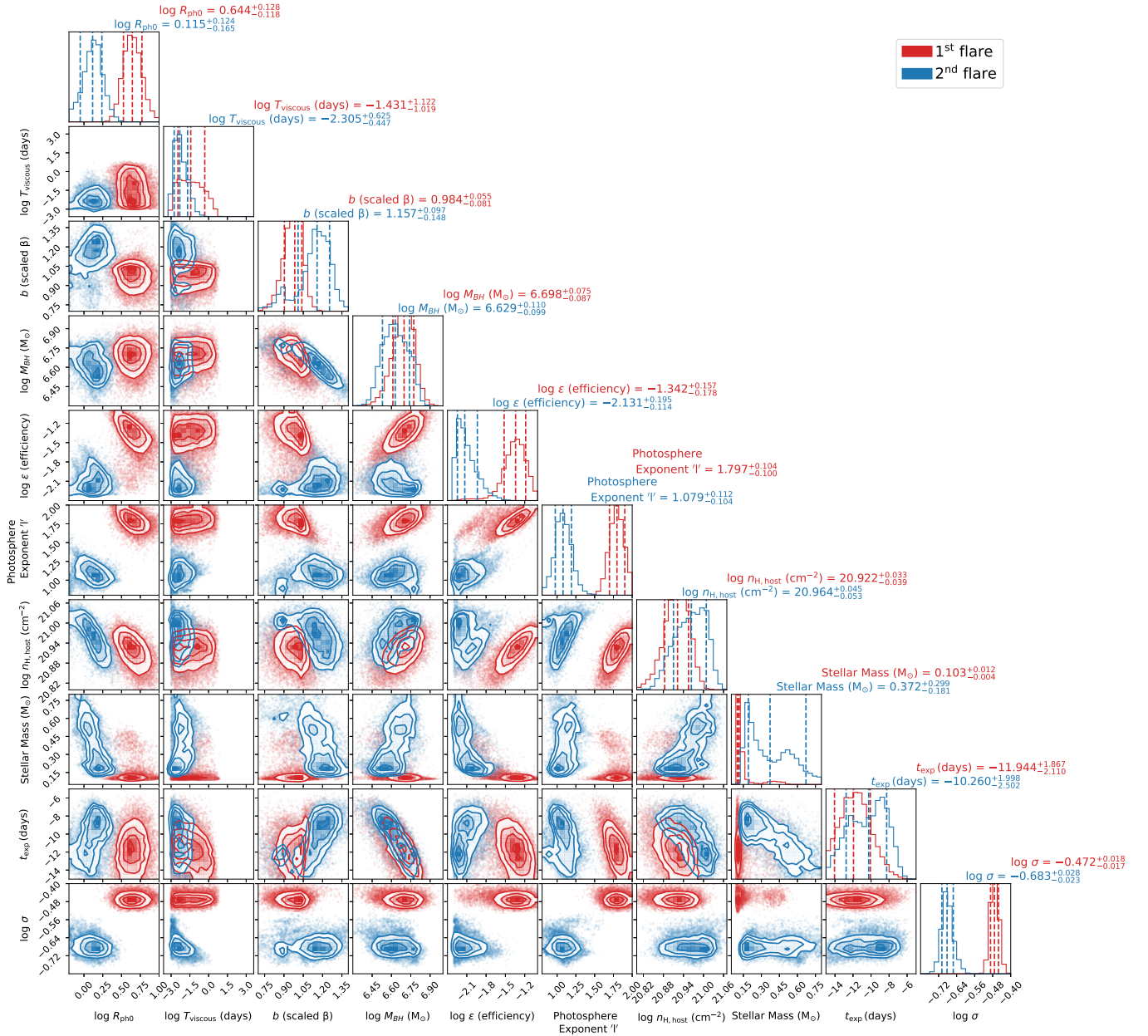


Figure 6. Two-dimensional posterior distributions of MOSFiT model fits for both the first (red) and second (blue) flare. While the black hole mass and host-galaxy extinction are consistent for both flares, the b parameter supports both a full and partial disruption for the first flare, while preferring a full disruption for the second flare.

100 Myr (median and 16th and 84th percentiles of the marginalized posterior distributions are given). The stellar mass reported by PROSPECTOR is the integral of the star formation history and so includes both stars and stellar remnants.

5. Discussion

5.1. AT 2022dbl Compared to Other TDEs

In the top panels of Figure 11, we compare the bolometric light curve of AT 2022dbl with those of the Bowen TDEs ASASSN-14li (T. W. S. Holoién et al. 2016), iPTF15af (N. Blagorodnova et al. 2019), iPTF16fnl (N. Blagorodnova et al. 2017; F. Onori et al. 2019), AT 2017eqx (M. Nicholl et al. 2019), AT 2018dyb (G. Leloudas et al. 2019), and AT 2019qiz (M. Nicholl et al. 2020) and with the well-sampled

non-Bowen optical-ultraviolet TDE ASASSN-14ae (T. W. S. Holoién et al. 2014). All bolometric light curves are derived from the best-fit blackbody parameters of each event. AT 2022dbl has the typical peak bolometric luminosities among Bowen TDEs, with decline rates consistent with the comparison sample.

In the bottom panel of Figure 11 and in Table 6, we compare the total radiated energy of each flare of AT 2022dbl between the earliest available data point (but no later than the peak) and 110 days after peak to those of TDEs with similar data coverage: PS1-10jh (S. Gezari et al. 2012), AT 2017eqx (M. Nicholl et al. 2019), AT 2018dyb (G. Leloudas et al. 2019), AT 2018hco (S. van Velzen et al. 2021), AT 2018hyz (S. van Velzen et al. 2021), AT 2018iih (S. van Velzen et al. 2021), AT 2018zr (S. van Velzen et al. 2021), AT 2019azh (S. Faris et al. 2024), AT 2019dsg (S. van Velzen et al. 2021),

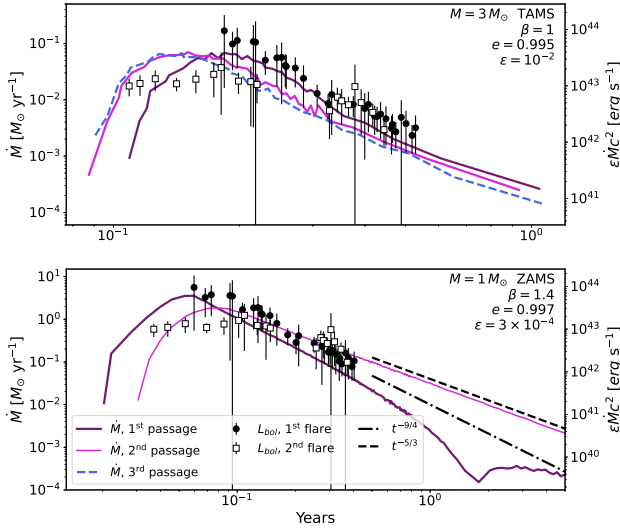


Figure 7. Mass fallback rates (left axes) are shown for the first, second, and third pericenter passages of a $3 M_{\odot}$ terminal-age main-sequence (TAMS) star on a bound orbit around a $10^6 M_{\odot}$ black hole having a pericenter distance of $R_p \sim R_t$ with eccentricity $e = 0.995$, consistent with an orbital period of ~ 700 days (top), and for the first and second pericenter passages of a $1 M_{\odot}$ zero-age main-sequence (ZAMS) star having a pericenter distance $R_p \sim R_t/1.4$ with an orbital eccentricity $e = 0.997$, consistent with the same orbital period. In the latter case, the star is fully disrupted on the second passage. The bolometric luminosities of the two flares (right axes) are overlaid with different efficiency parameters ϵ in each case to match the mass fallback rate, assuming the luminosity is entirely powered by mass fallback with a constant efficiency. The late-time bump in the $1 M_{\odot}$ first passage mass fallback rate is due to the less-bound debris returning after one orbital period and is much smaller than the fallback rate due to the bound debris from the second passage. The current data are not able to distinguish between these two types of scenarios. This could be determined by the existence of a third flare. Error bars denote 1σ uncertainties.

AT 2019ehz (S. van Velzen et al. 2021), AT 2019eve (S. van Velzen et al. 2021), and AT 2019qiz (M. Nicholl et al. 2020) on the same time range. While on the low side of emitted energies, each flare of AT 2022dbl is still within the range spanned by the comparison sample.

The top panel of Figure 4 shows that the blackbody radii of both flares of AT 2022dbl are at the extreme low end of the comparison sample. It is not known what sets the blackbody radius in optical-ultraviolet TDEs. According to the reprocessing emission picture, this radius could be related to the size of the reprocessing layer of material; however, the origin of the reprocessing material itself is not well understood. It is therefore not clear how to interpret the low inferred radii until more such events are discovered.

Further to the spectral comparison of Figure 8, which places AT 2022dbl in the He-rich Bowen TDE class (S. van Velzen et al. 2020), we compare the spectra near the peak luminosity of each flare of AT 2022dbl to those of the TDEs PTF09ge (I. Arcavi et al. 2014), which shows a similar He II emission profile and no $H\alpha$ emission, and iPTF16axa (T. Hung et al. 2017) and AT 2018dyb (G. Leloudas et al. 2019), which show similar N III emission profiles and varying $H\alpha$ strengths, in Figure 12. This comparison demonstrates how the similarity between the spectra of both flares of AT 2022dbl is striking compared to the ranges of spectra seen in TDEs. Specifically, both flares of AT 2022dbl exhibit identically weak $H\alpha$, in between the $H\alpha$ strengths seen in other TDEs.

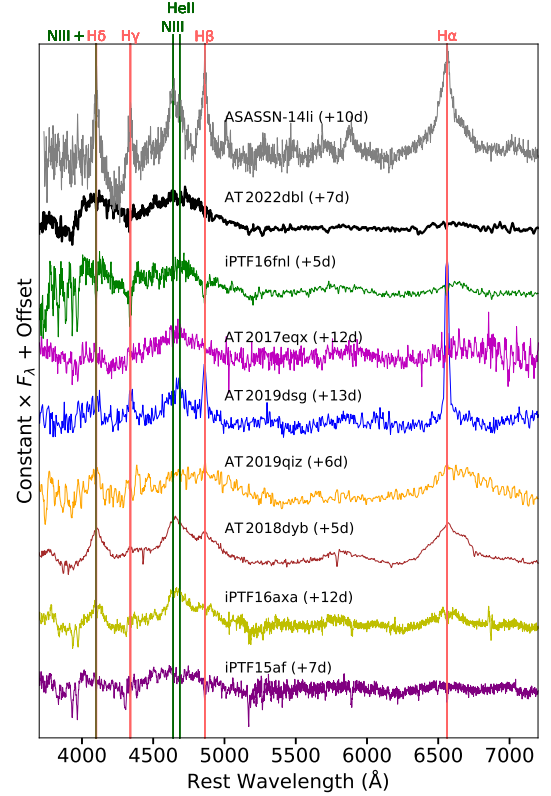


Figure 8. Spectroscopic comparison of AT 2022dbl with a sample of Bowen TDEs in similar phases with respect to peak luminosity. The spectra have been continuum-subtracted to highlight the emission features. AT 2022dbl is clearly a member of the Bowen TDE class.

5.2. Possible Origins of the Double Flare in AT 2022dbl

5.2.1. Gravitational Lensing

We perform two tests to check whether the two flares of AT 2022dbl could be two lensed images of the same TDE. First, we measure the ultraviolet-to-optical color evolution of both flares of AT 2022dbl (Figure 13), which shows that both flares evolve slightly differently. In a lensing scenario, different colors between images can be explained by different amounts of dust extinction along the different light paths. However, the color differences should be constant in time, which is not the case for AT 2022dbl. The slight difference in color evolution between the flares thus already strongly disfavors a lensing scenario for AT 2022dbl.

Second, we examine whether the two flares can be two time-delayed images of a single lensed TDE given the timescale between the two flares, their redshift, and the peak brightness ratio. Since both events have spectra that place them unambiguously at the redshift of the host, $z = 0.0284$, we primarily consider if there may be an intervening mass between us and the host to account for lensing. In what follows, we assume a point-mass lens. Other common alternatives (for example, a singular isothermal sphere lens) should lead to similar conclusions. The deflection angle at an angular distance θ from a point mass of mass M is given by $\alpha(\theta) = \frac{4GM}{c^2\theta} \frac{D_{ls}}{D_l D_s}$, where G is the gravitational constant and c is the speed of light. D_l , D_s , and D_{ls} are the angular diameter distances to the lens (located at z_l), to the source (located at z_s), and between the lens and the source, respectively. A

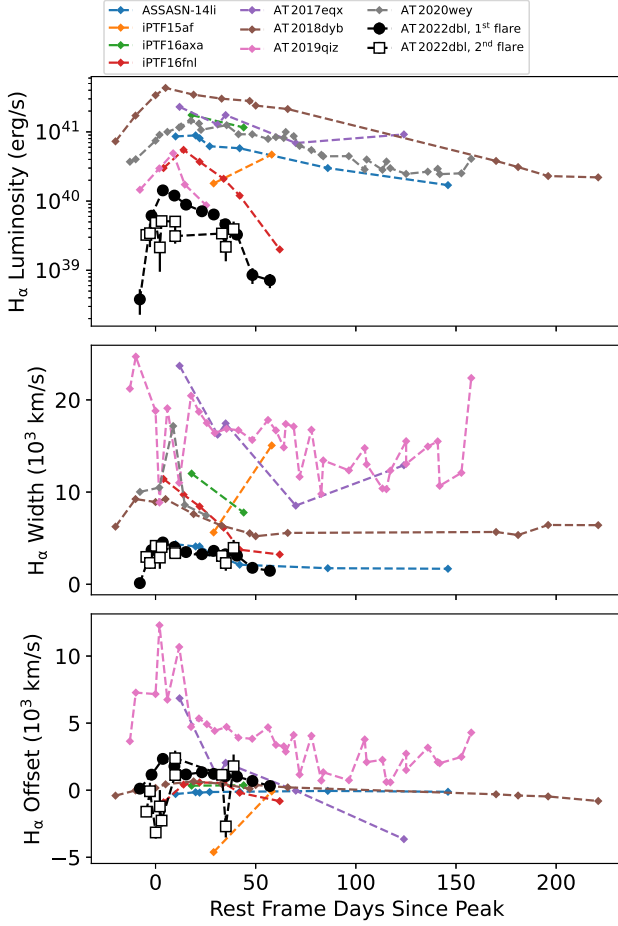


Figure 9. $H\alpha$ luminosity (top), FWHM (middle), and offset (bottom) evolution of AT 2022dbl, compared with those of a sample of TDEs. AT 2022dbl has the lowest $H\alpha$ luminosity and width of the sample consistently in both flares. Both flares are nearly identical in the $H\alpha$ width.

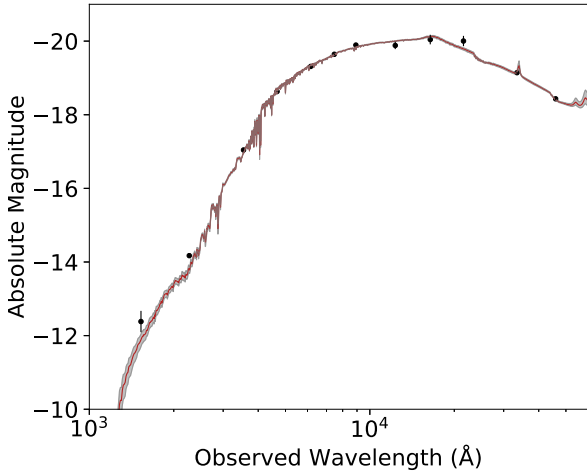


Figure 10. Our PROSPECTOR best-fit median model and 16th and 84th percentile ranges for the AT 2022dbl host-galaxy spectral energy distribution.

point-mass lenses would generally lead to two images appearing, one on each side of the lens. The magnification of the two images in this case is given by (P. Schneider et al. 1992)

$$\mu_{\pm} = \frac{u^2 + 2}{2u\sqrt{u^2 + 4}} \pm \frac{1}{2}, \quad (1)$$

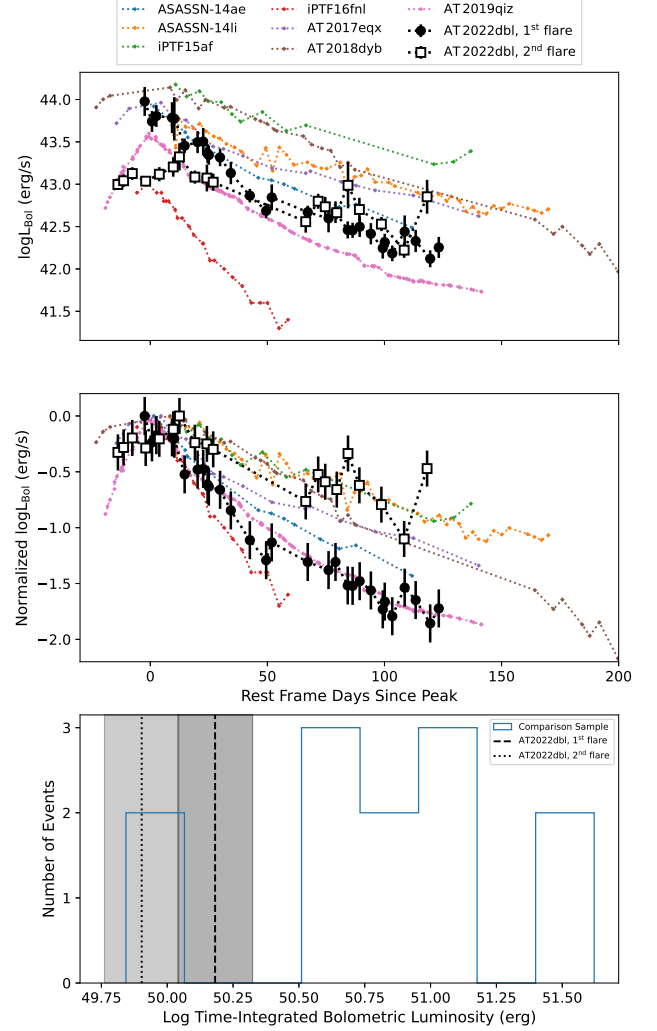


Figure 11. Compared to a sample of other Bowen TDEs, both flares of AT 2022dbl show typical peak bolometric luminosities (top) and decline rates (middle; same as top panel but normalized to the brightest point). The second flare of AT 2022dbl is fainter and shallower than the first. Error bars denote 1σ uncertainties. We also present the time-integrated bolometric luminosity (bottom) of each flare of AT 2022dbl (dashed lines) compared to those of optical-ultraviolet TDEs from the literature (see Table 6). Here we use only events with data between peak (or earlier) and 110 days postpeak, and we integrate between the first available point out to 110 days. AT 2022dbl shows relatively low emitted energy but within the range spanned by the comparison sample. Gray bands denote 1σ uncertainties around the AT 2022dbl values. All bolometric light curves are calculated from best-fit blackbody parameters.

where u is the angular separation of the source from the point mass in units of the Einstein angle, $u \equiv \beta\theta_E^{-1}$. The Einstein angle $\theta_E = \left(\frac{4GM}{c^2} \frac{D_{ls}}{D_1 D_s}\right)^{1/2}$ is the radial position of the ring that would form around a point (or circularly symmetric) lens were the source lying behind its center along the line of sight to it. The time delay between the two images in this case can be written as (P. Schneider et al. 1992)

$$\Delta t = \frac{4GM}{c^3} (1 + z_1) \tau(u), \quad (2)$$

where

$$\tau(u) = \frac{1}{2} u \sqrt{u^2 + 4} + \ln \frac{\sqrt{u^2 + 4} + u}{\sqrt{u^2 + 4} - u}. \quad (3)$$

Table 6
Integrated Bolometric Energy of TDEs Plotted in the Bottom Panel of Figure 11

Name	Time Range (days)	Integrated Energy (log(erg s ⁻¹))	References
PS1-10jh	[-78.6, 110.0]	51.6 ^{+0.1} _{-0.1}	S. Gezari et al. (2012)
AT 2017eqx	[-14.5, 110.0]	50.5 ^{+0.1} _{-0.1}	M. Nicholl (2018)
AT 2018dyb	[-23.1, 110.0]	50.9 ^{+0.1} _{-0.1}	G. Leloudas et al. (2019)
AT 2018hco	[-22.0, 110.0]	51.1 ^{+0.1} _{-0.1}	S. van Velzen et al. (2020)
AT 2018hyz	[0.0, 110.0]	50.7 ^{+0.1} _{-0.1}	S. van Velzen et al. (2020)
AT 2018iih	[-42.0, 110.0]	51.5 ^{+0.1} _{-0.1}	S. van Velzen et al. (2011)
AT 2018zr	[-23.0, 110.0]	50.6 ^{+0.1} _{-0.1}	S. van Velzen et al. (2020)
AT 2019azh	[-18.0, 110.0]	51.0 ^{+0.1} _{-0.1}	S. Faris et al. (2024)
AT 2019dsg	[-20.0, 110.0]	51.1 ^{+0.1} _{-0.1}	S. van Velzen et al. (2020)
AT 2019ehz	[-16.0, 110.0]	50.8 ^{+0.1} _{-0.1}	S. van Velzen et al. (2020)
AT 2019eve	[-5.0, 110.0]	49.8 ^{+0.1} _{-0.1}	S. van Velzen et al. (2020)
AT 2019qiz	[-19.2, 110.0]	50.0 ^{+0.1} _{-0.1}	M. Nicholl et al. (2020)
AT 2022dbl (Flare 1)	[0.0, 110.0]	50.2 ^{+0.1} _{-0.1}	This work
AT 2022dbl (Flare 2)	[-22.8, 110.0]	49.9 ^{+0.1} _{-0.1}	This work

Note. The integration time range is given in rest-frame days relative to peak.

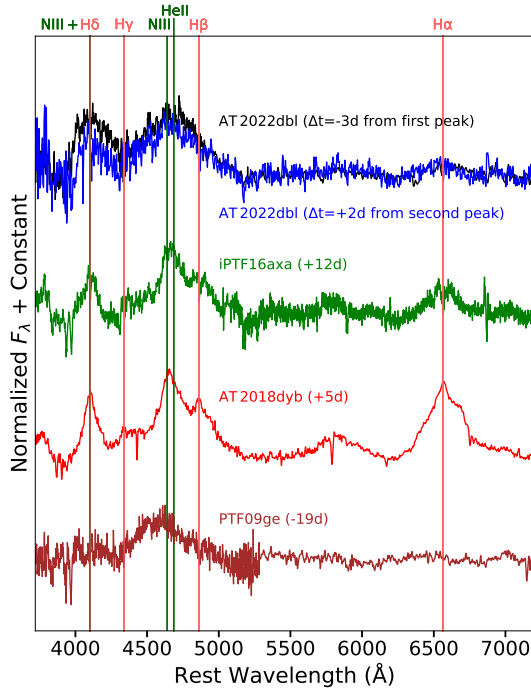


Figure 12. Continuum-subtracted spectra of AT 2022dbl near the peak luminosity of each flare compared to those of optical-ultraviolet TDEs from the literature. Phases are noted in rest-frame days relative to peak luminosity. The spectral features seen during both flares of AT 2022dbl are virtually identical to each other compared to the variability seen in the TDE population (especially regarding the H α strength).

For the following calculations, we assume a standard Λ CDM cosmology with $H_0 = 70 \text{ km s}^{-1} \text{ Mpc}^{-1}$, $\Omega_\Lambda = 0.7$, and $\Omega_m = 0.3$. We adopt an angular diameter distance of $D_s = 1.1751 \times 10^8 \text{ pc}$ to the source, which corresponds to $z = 0.0284$, and place a fiducial lens at $z = 0.01$, yielding $D_l = 4.2307 \times 10^7 \text{ pc}$. Using the above equations, we find that such an intervening point-mass lens should be as massive as $\sim 10^{13} M_\odot$ to explain the time delay (~ 700 days) and magnification ratio ($\sim 2:1$) of the two events, were they counterimages of the same lensed event. Given the low

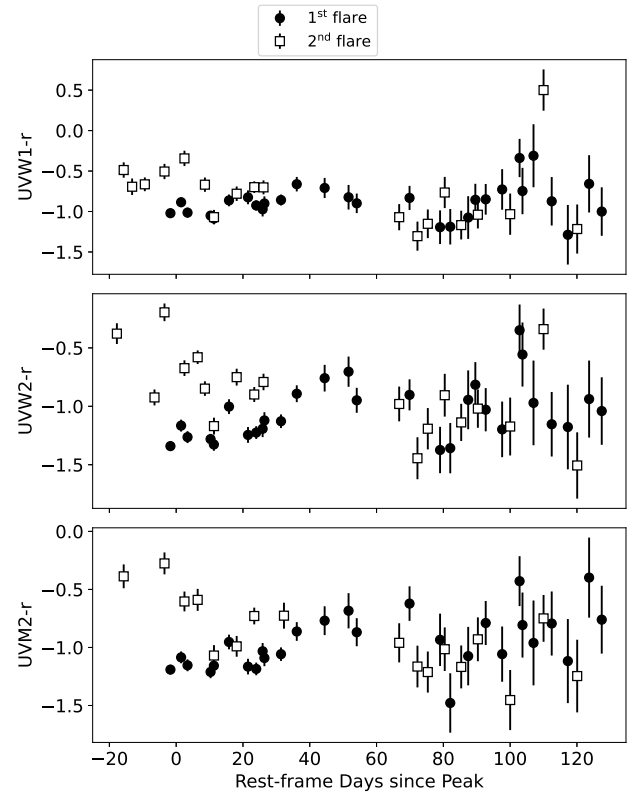


Figure 13. The ultraviolet-to-optical color evolution of both AT 2022dbl flares is roughly constant in time, as seen in other optical-ultraviolet TDEs. However, the small but significant differences in color evolution between the flares from peak luminosity to late times is enough to argue against both flares being two lensed images of the same underlying event.

redshift of the host and the lack of any optical signature of lensing or an intervening galaxy, it is not likely that such a lensing mass is found exactly between us and the host galaxy. This result does not strongly depend on the redshift of the fiducial intervening lens, and a similarly large mass is required even if the point lens is assumed to lie within the host galaxy. Similarly, any reasonably massive point lens within our galaxy

is also not capable in the above framework to generate images with sufficient time delay as observed.

We conclude that it is very unlikely that the two events are time-delayed images of the same lensed event but that they are instead most likely two separate events.

5.2.2. Two Unrelated TDEs

As stated above, the host galaxy of AT 2022dbl is a quiescent Balmer-strong galaxy. Such galaxies have been shown to have an enhanced TDE rate (I. Arcavi et al. 2014; K. D. French et al. 2016). More specifically, TDE rates in such galaxies correlate strongly with their Lick $H\delta_A$ index. We use the 15 optical TDEs with broad lines in their spectra (i.e., the same class of events as AT 2022dbl) from the K. D. French et al. (2020) TDE host-galaxy sample to estimate the probability of seeing two unrelated TDEs in a galaxy with a similar Lick $H\delta_A$ index as that of AT 2022dbl within 700 days of each other.

We obtain Lick $H\delta_A$ indices from the MPA-JHU catalogs of absorption line indices and emission line flux measurements (G. Kauffmann et al. 2003; J. Brinchmann et al. 2004; C. A. Tremonti et al. 2004) retrieved through the SDSS III Science Archive Server. We calculate the fraction of TDEs in three $H\delta_A$ bins (equally spaced between 1.3 and 6 Å with the host of AT 2022dbl belonging to the first, i.e., lowest $H\delta_A$, bin) relative to the fraction of galaxies in each bin. This gives us a TDE rate enhancement for each galaxy bin of $\times 10.09$, $\times 12.23$, and $\times 132.43$ (from the lowest $H\delta_A$ bin to the highest). We then multiply this enhancement factor by a global TDE rate between 10^{-5} and 10^{-4} events per galaxy per year (N. C. Stone et al. 2020). This gives us the TDE rate for each $H\delta_A$ bin, which we use, assuming Poisson statistics, to calculate the probability for two events to occur within 700 days of each other in that bin. We then multiply this number by the total number of TDEs discovered to date in that galaxy bin. We assume that 50 optical-ultraviolet TDEs have been discovered to date in all galaxy types and that they are distributed between galaxy types in the same way as in the K. D. French et al. (2020) sample.

We find that the probability of observing two unrelated TDEs within 700 days of each other in a galaxy sharing the same $H\delta_A$ bin as that of the AT 2022dbl host galaxy is 0.037%–0.368%, depending on the assumption of the global TDE rate (10^{-5} – 10^{-4} events per galaxy per year). For a recent global rate estimate of 3.2×10^{-5} events per galaxy per year (Y. Yao et al. 2023), the probability that the two flares of AT 2022dbl are of unrelated TDEs is 0.12%.

This result is not sensitive to the number of bins chosen (using four bins, we find 0.14%, and with five bins, we find 0.16%; the small sample of host galaxies precludes splitting the population into six bins as in that case, the bin containing the host of AT 2022dbl has zero galaxies in it, precluding a rate enhancement calculation for it). The small number statistics and uncertainty in the global TDE rate prohibit a precise chance coincidence calculation, but our results indicate that it is of order $\sim 0.01\%$ – 0.1% .

We repeat this analysis for AT 2020vdq, a recently claimed repeating TDE (J. J. Somalwar et al. 2025b) for which the $H\delta_A$ index of the host galaxy (J. J. Somalwar et al. 2025a) is 4.50 ± 0.13 Å (J. Somalwar 2025, private communication) and the time interval between the flares is 2.6 yr. We find that the probability of observing two unrelated TDEs for these

conditions is 0.86%–8.61%, depending on the assumption of the global TDE rate (10^{-5} – 10^{-4} events per galaxy per year). This is more than an order of magnitude larger than for AT 2022dbl. Thus, even if both flares of AT 2020vdq were TDEs, it is much less clear than for AT 2022dbl that these two TDEs are related to the disruption of the same star. We conclude that AT 2022dbl is a much more likely repeating TDE than AT 2020vdq.

In addition, we argue that the likelihood of both flares of AT 2022dbl being of unrelated TDEs is even lower considering the similarity of the $H\alpha$ properties of both flares, compared to the spread of properties in a comparison sample of H-rich TDEs (Figure 9). For two unrelated stars to produce the same $H\alpha$ properties would imply that these properties are set mainly by the black hole rather than by the disrupted stars or their orbits. While it is not known what sets the properties of $H\alpha$ lines in TDEs, if they were driven primarily by the black hole, we would expect to see a correlation between $H\alpha$ emission properties and black hole properties across TDEs. However, this is not seen. The presence of $H\alpha$ in a TDE spectrum does not correlate with black hole mass (M. Nicholl et al. 2022), and when $H\alpha$ is present, neither does its width (P. Charalampopoulos et al. 2023) or luminosity (Figure 14). This suggests that at least the $H\alpha$ characteristics of a TDE must be influenced by its stellar and/or orbital properties and hence that such similar spectra are difficult to explain as coming from two unrelated disruptions. Together with the rate argument above, we conclude that both flares of AT 2022dbl must relate to the same TDE.

5.2.3. A Single TDE around an SMBH Binary

It has been suggested that post-starburst TDE host galaxies could be postmerger galaxies harboring a binary SMBH in their center. However, while a binary black hole can significantly increase the TDE rate (X. Chen et al. 2009; C. Wegg & J. Nate Bode 2011), such systems have been disfavored as the dominant drivers of enhanced TDE rates in post-starburst galaxies due to the timescales involved (K. D. French et al. 2017; N. C. Stone et al. 2019). In addition, for AT 2022dbl to be caused by an SMBH binary, the orbital period of the SMBH binary would have to be comparable to 700 days, as this is the only timescale over which the presence of the secondary black hole would significantly modify the dynamics of the debris (the debris exiting the Hill sphere of the primary yields a comparable estimate; E. R. Coughlin & P. J. Armitage 2018). In this case, a total black hole mass of $10^6 M_\odot$ implies a binary semimajor axis that is well within the sphere of influence of each black hole (since the semimajor axis scales as $M_{\text{BH}}^{1/3}$ for a given period, changes in the total mass at the order-of-magnitude level do not result in significant changes to the semimajor axis). While the cross section for tidal disruption is increased due to the larger geometrical area of the binary, at these small separations, the TDE rate would be enhanced by a factor of ~ 2 at most, since such a binary would cause the majority of stars to be ejected prior to disruption (E. R. Coughlin et al. 2017; S. Darbha et al. 2018). Therefore, the double flare of AT 2022dbl does not necessarily favor binary black holes as the drivers of enhanced TDE rates in post-starburst galaxies.

Still, we check whether the second outburst of AT 2022dbl could be due to a companion black hole. While the secondary black hole does generate stochasticity in the

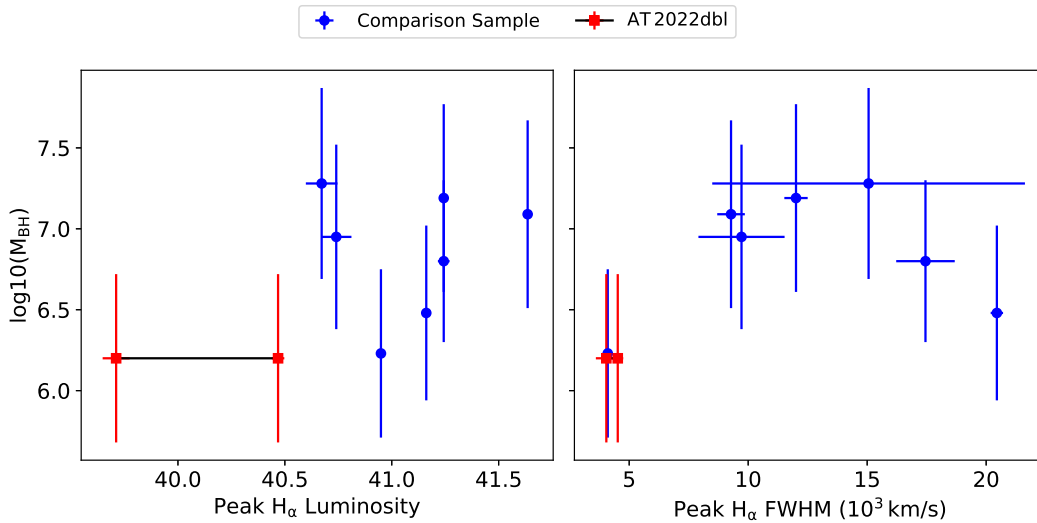


Figure 14. Black hole mass vs. TDE $H\alpha$ luminosity (left) and FWHM (right) around peak bolometric luminosity for AT 2022dbl (red) and the comparison sample in Figure 9 (blue). We do not find any strong correlations between black hole mass and $H\alpha$ luminosity or width, indicating that the similarity of the $H\alpha$ properties of the two AT 2022dbl flares is not solely related to the SMBH but is related to the star and/or its orbit. This strengthens the claim that the two flares of AT 2022dbl are related to the same star.

accretion rate onto the primary, this is usually at the expense of producing a sudden drop in the accretion rate (A. Ricarte et al. 2016), which is not observed here. Furthermore, we would expect the second brightening to be much less energetic than the first, also not observed here, owing to the fact that the amount of mass supplied to the black hole (i.e., the fallback rate) is itself much smaller at later times.

Alternatively, it could be that the second flare was due to the accretion of material by the secondary black hole. Again, however, we would expect the flare amplitude (or at least the total energy liberated) to be much lower than in the first flare, because the ejecta from the disruption by the primary black hole would be highly geometrically extended and the total mass available to the secondary black hole considerably reduced. It is also difficult to see why the second accretion event would be spectroscopically nearly identical to the first, given that the geometry of the accretion flow and the accretion rate would be different.

We conclude that the double flare of AT 2022dbl and its occurrence in a post-starburst galaxy do not constitute evidence for the presence of an SMBH binary.

5.2.4. Emission from the Less-bound Debris Tail

A star on a parabolic orbit that is disrupted (partially or completely) produces two tidal tails of debris, one of which is bound while the other is unbound. The reason for this is that the tidal field imparts a spread in the specific Keplerian energy of

$$\Delta\epsilon \simeq \frac{GM_*}{R_*} \left(\frac{M_{\text{BH}}}{M_*} \right)^{1/3} \quad (4)$$

(where M_* is the mass of the disrupted star and R_* is its radius) to the debris as the star passes through the tidal disruption radius (J. H. Lacy et al. 1982), meaning that the most-unbound debris has a specific energy $+\Delta\epsilon$. Equation (4) relies on the assumption that the star is approximately hydrostatic as it passes through the tidal radius. This spread in energy has been verified by a number of numerical

investigations when the star is described by a 5/3 polytrope and is completely destroyed (G. Lodato et al. 2009; J. Guillochon & E. Ramirez-Ruiz 2013; E. Steinberg et al. 2019; S. M. J. Norman et al. 2021), but it is less clear that it should hold for partial disruptions or different stellar structures.

When the star is bound to the black hole by an amount ϵ_c (i.e., ϵ_c is the specific energy of the surviving core), this energy barrier must be overcome to completely unbind material from the black hole, meaning that the most-unbound (or “least-bound,” if the specific energy is ultimately negative) material has a specific energy $\epsilon = \epsilon_c + \Delta\epsilon$. This implies that the ratio of $\epsilon_c/\Delta\epsilon$ is a measure of the importance of the specific energy of the core: if $\epsilon_c/\Delta\epsilon \ll 1$, then the core binding energy is unimportant, and the system is effectively parabolic (as concerns the ejection of mass on hyperbolic trajectories), whereas if $\epsilon_c/\Delta\epsilon \gg 1$, the entire stream is bound to the black hole (K. Hayasaki et al. 2018). Adopting an orbital period of 700 days and a black hole mass of $M_{\text{BH}} = 10^6 M_\odot$, the energy–period relationship of a Keplerian orbit gives $\epsilon_c \simeq -15GM_*/R_*$ for a solar-like star. Since $\Delta\epsilon = 100GM_*/R_*$, we would expect at most $\sim 15\%$ of the “unbound” tail to be gravitationally bound to the black hole (this is an upper limit, as some fraction of the material will accrete back onto the star). Because the return time of the debris must be at least as long as the orbital period of the star, a very firm upper limit on the accretion rate onto the black hole from the less-bound tail is (again, for a solar-like star) $\sim 0.07 M_\odot / (700 \text{ days}) \simeq 0.05 M_\odot \text{ yr}^{-1}$. This is approximately 2 orders of magnitude below the peak from the main flare (see Figure 7), implying that the second flare cannot—barring extreme changes to the accretion efficiency of the black hole—be due to the less-bound debris.

5.2.5. The Repeated Disruption of the Same Star

Having disfavored gravitational lensing of the same TDE, two unrelated TDEs, a single TDE around an SMBH binary, and the accretion from a debris tail; given the photometric and spectroscopic similarity of the two flares; and having presented analytical and numerical models that are consistent with the two flares arising from the disruption of the same star, we

conclude that AT 2022dbl is most likely the repeated disruption of the same star, with at least the first disruption being partial.

5.3. Dynamical Scenario for the Creation of AT 2022dbl

For a black hole of mass $M_{\text{BH}} \approx 10^6\text{--}10^{6.7} M_{\odot}$, a 700 day orbit implies a semimajor axis a of $2.3\text{--}4.0 \times 10^{15}$ cm. This is much smaller than the radius of influence of the black hole (which, for the host galaxy of AT 2022dbl, is $\sim 3\text{--}7 \times 10^{18}$ cm), from where most disrupted stars originate, and tidal dissipation alone cannot bind the star to the black hole sufficiently tightly to produce a 700 day period (M. Cufari et al. 2022).

Instead, the star could have been captured through the Hills mechanism (J. G. Hills 1988). According to this mechanism, the center of mass of a binary star system with mass M_b and separation a_b approaches the SMBH on an orbit with a pericenter distance smaller than $R_a = a_b \left(\frac{M_{\text{BH}}}{M_b}\right)^{1/3}$. At that distance from the SMBH, the binary is disrupted, with one star becoming unbound and ejected from the system and the other star remaining bound to the black hole. The bound star is expected to have an orbital period $\lesssim 10$ yr (see below), consistent with the period measured here.

For any mass to be removed from the star, the pericenter distance of its orbit R_p should be $\lesssim 2$ times the stellar tidal disruption radius (E. R. Coughlin & C. J. Nixon 2022), $R_t = R_* \left(\frac{M_{\text{BH}}}{M_*}\right)^{1/3}$. While this is typically smaller than the binary tidal disruption radius R_a , the captured star could be put onto such an orbit directly by the Hills mechanism (M. Cufari et al. 2022), or it could shrink its orbit and increase its eccentricity after being captured through two-body scatterings (see below).

Another way to produce the 700 day orbit is through eccentric Kozai–Lidov oscillations (Y. Kozai 1962; M. L. Lidov 1962) from an SMBH binary combined with two-body relaxation (D. Melchor et al. 2024). In this scenario, the second black hole would most likely be at separations of order the radius of influence from the disrupting black hole and therefore would not affect the observed flare, only the dynamics leading up to disruption.

5.3.1. The Orbital Period of AT 2022dbl

The difference between the observed light-curve peaks ΔT_{obs} , assuming that the luminosity tracks the fallback rate, is $\Delta T_{\text{obs}} = T_{\text{orb}} - T_{\text{peak},1} + T_{\text{peak},2}$, where $T_{\text{peak},1}$ and $T_{\text{peak},2}$ are the times to reach the peak fallback rate following the first and second pericenter passage of the star, respectively. These two times will not be identical because the star has imparted rotation (T. Ryu et al. 2020b; A. Bandopadhyay et al. 2024) and loses mass upon being partially disrupted. Hence, the orbital period of the star can only be approximated from the time between peaks (the observation of the sudden shutoff of emission, on the other hand, could directly constrain the time at which the star reaches pericenter; T. Wevers et al. 2023).

That being said, we now show that a period of ~ 700 days is consistent with theoretical expectations from the Hills mechanism. The tidal radius of a binary star system with semimajor axis a_b and total mass M_b is

$$R_a = a_b \left(\frac{M_{\text{BH}}}{M_b}\right)^{1/3}. \quad (5)$$

As the binary is ripped apart, one of the stars is captured on an orbit that has a specific binding energy about the black hole of

$$\epsilon_* = \frac{GM_b}{a_b} \left(\frac{M_{\text{BH}}}{M_b}\right)^{1/3}. \quad (6)$$

This then yields a period of the captured star of

$$T_* = \frac{\pi}{\sqrt{2}} \frac{GM_{\text{BH}}}{\epsilon_*^{3/2}} \simeq \frac{a_b^{3/2}}{\sqrt{GM_b}} \left(\frac{M_{\text{BH}}}{M_b}\right)^{1/2}. \quad (7)$$

For the binary to avoid being disrupted before reaching R_p , we require (G. D. Quinlan 1996)

$$\sqrt{\frac{GM_b}{a_b}} \gtrsim \sigma \Rightarrow a_b \lesssim \frac{GM_b}{\sigma^2}, \quad (8)$$

where σ is the velocity dispersion of the stars in the nucleus of the galaxy. Combining this with Equation (7) yields

$$T_* \lesssim \frac{GM_b}{\sigma^3} \left(\frac{M_{\text{BH}}}{M_b}\right)^{1/2}. \quad (9)$$

Adopting an $M_{\text{BH}}\text{--}\sigma$ relation of the form (D. Merritt 2000)

$$M_{\text{BH}} = M_0 \left(\frac{\sigma}{\sigma_0}\right)^n \Rightarrow \sigma = \sigma_0 \left(\frac{M_{\text{BH}}}{M_0}\right)^{1/n}, \quad (10)$$

the equation for T_* becomes

$$T_* \lesssim \frac{G\sqrt{M_b}}{\sigma_0^3} \left(\frac{M_{\text{BH}}}{M_0}\right)^{-3/n} M_{\text{BH}}^{1/2}, \quad (11)$$

which can be rewritten as

$$T_* \lesssim \frac{G\sqrt{M_b M_0}}{\sigma_0^3} \left(\frac{M_{\text{BH}}}{M_0}\right)^{\frac{n-6}{2n}}. \quad (12)$$

Recent estimates of the $M_{\text{BH}}\text{--}\sigma$ relation give $n = 5.1$, $M_0 = 1.9 \times 10^8 M_{\odot}$, and $\sigma_0 = 200 \text{ km s}^{-1}$ (N. J. McConnell et al. 2011). This then gives

$$T_* \lesssim 7.2 \left(\frac{M_b}{M_{\odot}}\right)^{1/2} \left(\frac{M_{\text{BH}}}{M_0}\right)^{-3/34} \text{ yr}. \quad (13)$$

This suggests that there could be many objects with periods longer than the ~ 700 day orbit of AT 2022dbl, and that the binary that produced the captured star was particularly hard, i.e., with a semimajor axis significantly smaller than $\sim GM_b/\sigma^2$. In addition, Equation (6) is the most likely value, and while binding energies larger than this are rare, there could be a substantial number (M. Cufari et al. 2022) of captured objects with periods that are even longer than the limit in Equation (13).

Changes to the orbital period could be achieved by imparting energy—through either rotation or internal/oscillatory modes—to the surviving core. This effect is important when the imparted energy is comparable to (or at least not too dissimilar from) the binding energy of the core to the black hole. In terms of the orbital period T , the latter is $\epsilon_c = (2\pi GM_{\text{BH}}/T)^{2/3}/2$, which for $M_{\text{BH}} = 10^6 M_{\odot}$ and $T = 700$ days is $\epsilon_c \simeq 3 \times 10^{16} \text{ erg g}^{-1}$. The energy imparted via tides can at most be equal to the binding energy of the star, meaning that the change in the specific energy satisfies

$\Delta\epsilon \leq \epsilon_* \simeq GM_*/R_* \simeq 2 \times 10^{15} \text{ erg g}^{-1}$, where we adopted a mass–radius relationship $R_* = R_\odot (M_*/M_\odot)$ for a main-sequence star (O. Demircan & G. Kahraman 1991). The ratio of the energy imparted via tides to the binding energy of the orbit is therefore $\lesssim 1/15$, but this is likely a substantial overestimate, given that the mass powering the accretion is a very small fraction of a solar mass. In the limit where the star is effectively at the partial disruption radius and a low amount of mass is stripped, the change in the binding energy of the star is (M. Cufari et al. 2023) $\Delta\epsilon \simeq 1\% \epsilon_*$, and we would therefore expect the relative change in the period to be $\Delta T/T \simeq -3/2 \times \Delta\epsilon/\epsilon_c \simeq 0.1\%$, implying an absolute change in the orbital period of $\Delta T \lesssim 1$ day.

5.3.2. Formation of AT2022dbl through the Hills Mechanism and Angular Momentum Relaxation

With an orbital period of $T_* \approx 700$ days and a pericenter distance R_p comparable to the tidal disruption radius R_t , the orbital eccentricity is constrained to

$$\begin{aligned}
 1 - e &\approx \beta_*^{-1} (2\pi)^{2/3} \frac{R_*}{(GM_* T_*^2)^{1/3}} \\
 &\approx 0.006 \left(\frac{T_*}{700 \text{ days}} \right)^{-2/3} \left(\frac{R_*}{R_\odot} \right) \left(\frac{M_*}{M_\odot} \right)^{-1/3} \left(\frac{\beta_*}{0.5} \right)^{-1}, \quad (14)
 \end{aligned}$$

where we normalize to $\beta_* \equiv R_t/R_p = 0.5$ as the penetration factor appropriate for a partial disruption. On the other hand, stars in a binary of mass M_b captured via the Hills mechanism typically have an eccentricity of approximately (M. Cufari et al. 2022)

$$\begin{aligned}
 1 - e_{\text{Hills}} &\approx \frac{2}{\beta_b} (M_b/M_{\text{BH}})^{1/3} \\
 &\approx 0.025 \beta_b^{-1} \left(\frac{M_{\text{BH}}}{10^6 M_\odot} \right)^{-1/3} \left(\frac{M_b}{2 M_\odot} \right)^{1/3}, \quad (15)
 \end{aligned}$$

where here we normalize to a penetration factor for the binary $\beta_b \equiv R_a/R_p = 1$ (here R_p is the pericenter distance of the binary from the black hole), as the tidal splitting of binaries in galactic nuclei is typically governed by an empty loss-cone regime (N. C. Stone et al. 2020).

Thus, either the binary penetration factor β_b is roughly 4 or the orbital eccentricity of the captured star needs to be excited from its initial value to its value inferred at disruption (Equation (14)). This can happen through two-body scatterings with other field stars, a process that would occur over the angular momentum relaxation time of approximately (D. Merritt 2013)

$$\begin{aligned}
 \tau_{2B}^J &\approx \frac{P_{\text{orb}}}{2\pi N_*(R_a)} \left(\frac{M_{\text{BH}}}{M_*} \right)^2 (\ln\Lambda)^{-1} (1 - e_{\text{Hills}}) \\
 &\approx 5 \times 10^6 \text{ yr} \left(\frac{P_{\text{orb}}}{700 \text{ days}} \right)^{1/6} \left(\frac{\ln\Lambda}{10} \right)^{-1} \left(\frac{M_{\text{BH}}}{10^6 M_\odot} \right)^{0.18}, \quad (16)
 \end{aligned}$$

where $N_*(R_a)$ is the number of stars of semimajor axis comparable to R_a and $\ln\Lambda \approx \ln M_{\text{BH}}/M_* \approx 10$ is the Coulomb logarithm. Here we assume a Bahcall–Wolf density profile

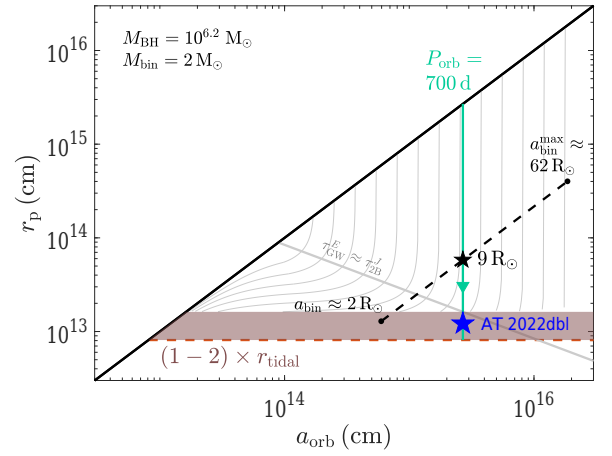


Figure 15. Illustration of a possible Hills mechanism formation channel for AT2022dbl. Orbits of a binary star system of total mass $M_{\text{bin}} = 2 M_\odot$ near a black hole of mass $M_{\text{BH}} = 10^{6.2} M_\odot$ are shown in a phase space of pericenter distance (r_p) vs. semimajor axis (a_{orb}). The solid black diagonal line at $r_p = a_{\text{orb}}$ corresponds to circular orbits ($e = 0$), while eccentric orbits lie below this line. The vertical green line denotes the approximate semimajor axis of AT2022dbl, the shaded red region is its pericenter distance (see text for details), and the blue star denotes their intersection. The black dashed diagonal line corresponds to the typical orbits of stars captured by the Hills mechanism, spanned by the range of possible binary separations a_{bin} , from contact binaries ($a_{\text{bin}} \approx 2 R_\odot$) to binaries on the soft/hard boundary given by the galactic velocity dispersion ($a_{\text{bin}} \approx 62 R_\odot$). A binary of intermediate separation, $a_{\text{bin}} \approx 9 R_\odot$, marked by the black star, would result in an orbital period similar to that of AT2022dbl yet with $r_p \approx 10$ times the tidal radius. Angular momentum relaxation through two-body scatterings could excite the captured star’s eccentricity without undergoing substantial changes in energy (and hence in a_{orb}), bringing it toward the tidal radius on a nearly vertical track in this phase space (denoted by the green arrow). Thin gray lines show steady-state trajectories in this phase space, due to the combined effect of two-body relaxation and gravitational-wave inspiral. Well above the thick gray line, orbits evolve primarily due to relaxation along mostly vertical tracks, while below this line, gravitational-wave evolution is more rapid, and orbits follow a nearly horizontal trajectory.

(J. N. Bahcall & R. A. Wolf 1977), such that $N_*(R_a) \approx (M_{\text{BH}}/M_*) (R_a/GM_{\text{BH}}/\sigma^2)^{5/4}$, and the $M_{\text{BH}}-\sigma$ relation of J. Kormendy & L. C. Ho (2013). For the orbital parameters relevant here, this time is shorter than the circularization time due to gravitational waves, which is given by (P. C. Peters 1964)

$$\begin{aligned}
 \tau_{\text{GW}}^E &\approx \frac{12\sqrt{2}}{85} \frac{GM_{\text{BH}}}{c^3} \frac{M_{\text{BH}}}{M_*} \left(\frac{a}{GM_{\text{BH}}/c^2} \right)^4 (1 - e_{\text{Hills}})^{7/2} \\
 &\approx 4 \times 10^9 \text{ yr} \beta_b^{-7/2} \left(\frac{M_{\text{BH}}}{10^6 M_\odot} \right)^{-11/6} \left(\frac{P_{\text{orb}}}{700 \text{ days}} \right)^{8/3}. \quad (17)
 \end{aligned}$$

Thus, the orbit will not undergo substantial changes in energy and period during its angular momentum relaxation to higher eccentricity. The hierarchy $\tau_{2B}^J < \tau_{\text{GW}}^E$ is maintained even as e increases to the (partial) disruption of the star, since $\tau_{2B}^J/\tau_{\text{GW}}^E \propto (1 - e)^{-5/2}$, such that as $(1 - e)$ decreases by a factor of ~ 4 , the timescale ratio increases by a factor of ~ 32 . This process is illustrated in Figure 15.

In summary, assuming a Sun-like star captured from a binary system with a mass ratio of ~ 1 by the Hills mechanism around a $10^6 M_\odot$ black hole, the following orbital parameters can reproduce a system like AT2022dbl. For a velocity dispersion $\sigma = 200 \text{ km s}^{-1}$ in the galaxy nucleus, the

maximum allowed semimajor axis for the binary to survive down to the black hole is (Equation (8)) $a_b \lesssim 6.7 \times 10^{11}$ cm. The tidal radius for disrupting such a binary is then (Equation (5)) $\lesssim 5.3 \times 10^{13}$ cm. The captured star would then have entered an orbit at a pericenter distance of 1.4×10^{13} cm, which is twice its tidal disruption radius $R_t = R_*(M_{\text{BH}}/M_*)^{1/3} = 7 \times 10^{12}$ cm, to undergo a partial disruption with penetration factor $\beta_* = 0.5$. This would entail an eccentricity of $e = 0.993$ (Equation (14)), making the semimajor axis $a = R_p/(1 - e) = 2.3 \times 10^{15}$ cm, corresponding to a period of $P = 2\pi a^{3/2}/\sqrt{GM_{\text{BH}}} = 700$ days, as observed.

The formation of such systems to begin with is governed by the scattering rate of binaries in galactic nuclei onto highly eccentric orbits, leading to their tidal split-up. If binaries of the relevant range of orbital separations constitute a fraction f_b of all stars within the black hole’s sphere of influence, the formation rate of such systems will be approximately $f_b \mathcal{R}_{\text{TDE}}$, where \mathcal{R}_{TDE} is the overall TDE rate. Systematic classification of full versus repeating TDEs will thus be useful in constraining the dynamics and demographics of stellar populations within galactic nuclei.

5.4. Implications

The similarity of AT 2022dbl to the class of optical-ultraviolet TDEs in its total energy, temperature, spectral features, and host-galaxy characteristics raises the question of whether all members of the class are in fact partial disruptions (as also tentatively suggested by C. Liu et al. 2025).

The existence of multiple flares of similar radiated energy in a seemingly normal TDE has clear implications for the missing energy problem in optical-ultraviolet TDEs. AT 2022dbl suggests that the total radiated energy in other TDEs may currently be underestimated given the uncertain recurrence times and number of flares associated with a given optical-ultraviolet TDE.

Alternatively, it could be that both full and partial disruptions emit almost the same amount of energy in radiation with nearly identical emission properties. This could happen if the luminosity of the accretion flow is roughly limited by the Eddington luminosity, even if the accretion rate is not. Indeed, depending on the black hole mass assumed for AT 2022dbl, the first flare could be Eddington-limited.²⁶ The luminosities of other TDEs are also comparable to the Eddington luminosity for the more common low-mass black holes (Y. Yao et al. 2023), and the theoretically predicted fallback rates are super-Eddington (M. J. Rees 1988). If this is the case, it can solve the missing energy problem through super-Eddington accretion in which the energy goes into the black hole and outflows, rather than into radiation. In this interpretation, the distinguishing feature between partial and complete disruption would primarily be the postpeak decline rate (being steeper for partial disruptions), which is consistent with both the observations presented here and theoretical predictions (M. J. Rees 1988; E. S. Phinney 1989; J. Guillochon & E. Ramirez-Ruiz 2013; E. R. Coughlin & C. J. Nixon 2019; J. Krolik et al. 2020; A. Bandopadhyay et al. 2024).

Indeed, both flares have similar light curves, with the second being fainter and having a shallower postpeak decline ($\sim t^{-5/3}$)

²⁶ Using the host-galaxy black hole estimate, we find a peak Eddington ratio of $0.47_{-0.32}^{+1.11}$ for the first flare. The lower black hole mass estimates from TDEMass imply an even higher ratio.

than the first ($\sim t^{-2.7}$). However, it is not possible to determine whether the second flare continued to decline at this rate or whether it simply had a broader peak and its decline rate later steepened to resemble that of the first flare.

This leads to two possibilities regarding the fate of the star and future flares of AT 2022dbl: either both disruptions were partial or the first was partial and the second was the full disruption of the star. The existence of a third flare (possibly very similar to the first two; top panel of Figure 7) in early 2026 will determine whether the second flare was also due to a partial disruption or whether the second flare could have been the full disruption of the star.

The first possibility implies that all optical-ultraviolet TDEs, regardless of initial luminosity decline rate, could be partial disruptions, while the second possibility implies that only some optical-ultraviolet TDEs are partial disruptions, exhibiting similar observational properties as full disruptions. Whichever turns out to be the correct interpretation, it will have far-reaching implications for our understanding of TDEs, since most models to date assume that all optical-ultraviolet TDEs are full disruptions (an assumption ruled out here by either interpretation).

6. Summary and Conclusions

We presented and analyzed observations of the double-flare TDE AT 2022dbl. The spectral features, blackbody temperature, luminosity, and total integrated energy of each flare of AT 2022dbl are typical of the optical-ultraviolet TDE class (S. van Velzen et al. 2020; E. Hammerstein et al. 2023), as are the radio detections from shortly after optical discovery (indicating a subrelativistic outflow with no luminous delayed radio flares in the first 2 yr; K. D. Alexander et al. 2016; A. Hoesch et al. 2021a). The host galaxy of AT 2022dbl is a quiescent Balmer-strong galaxy, which is also typical of optical-ultraviolet TDE hosts (I. Arcavi et al. 2014; K. D. French et al. 2020), and was even preselected 4 yr before the discovery of AT 2022dbl as a likely TDE host (K. D. French & A. I. Zabludoff 2018).

Thus, all of the characteristics of AT 2022dbl place it in the class of optical-ultraviolet TDEs without being an outlier in any parameter, except for having a second flare approximately 700 days after the first flare. We show that the second flare exhibits a very similar light curve (albeit fainter and with a slower postpeak decline in the ultraviolet bands) and nearly identical spectra as the first flare.

Given the time separation and slight differences in ultraviolet-to-optical color evolution between the two flares, we are able to rule out that the two flares are due to gravitational lensing of a single TDE. Our analysis of the host galaxy of AT 2022dbl strongly disfavors two unrelated TDEs as the origin of the two flares, and the light curves of both flares disfavor the disruption of the same star by two different SMBHs. We presented both analytical and numerical models that are consistent with the scenario of both flares being the disruption of the same star by the same SMBH, with at least the first flare being due to a partial disruption of the star. We have further presented a possible dynamical scenario that can reproduce the disruption parameters.

We conclude that AT 2022dbl represents two consecutive disruptions of the same star, which is on a bound orbit (with an orbital period of approximately 700 days) about an SMBH and for which at least the first flare was the result of a partial

disruption. Given that until now, candidate repeating partial disruptions were either for events with spectra and light curves not typical of the optical-ultraviolet TDE class, for events for which optical spectra or photometry were not taken during one of the flares, or for events in host galaxies capable of producing multiple TDEs on the observed timescales, we determine that AT 2022dbl is the first robust case of a partial disruption appearing as an otherwise “normal” optical-ultraviolet TDE.

As such, this has far-reaching implications for the class of optical-ultraviolet TDEs as a whole. It is possible that other members of this class (or even all of them) are also partial disruptions, just on longer return timescales (or of stars on single passes). If this is the case, it requires a reassessment of the emission mechanisms, rates, and processes driving the host-galaxy preference of optical-ultraviolet TDEs.

Acknowledgments

This research was supported in part by grant NSF PHY-2309135 to the Kavli Institute for Theoretical Physics (KITP), where part of this work was done, during the “Toward a Physical Understanding of Tidal Disruption Events” program. We are grateful to Ashish Meena for helpful discussion and to the anonymous referee for useful comments.

L.M. acknowledges support through a UK Research and Innovation Future Leaders Fellowship (grant No. MR/T044136/1). Support for L.M. at Tel Aviv University was provided by the European Research Council (ERC) under the European Union’s Horizon 2020 research and innovation program (grant agreement No. 852097). I.A. acknowledges support from the ERC under the European Union’s Horizon 2020 research and innovation program (grant agreement No. 852097), from the Israel Science Foundation (ISF; grant No. 2752/19), from the United States–Israel Binational Science Foundation (BSF; grant No. 2018166), and from the Pazy foundation (grant No. 216312). M.N., M.A., J.F., D.A.H., C.M., E.P.G., and G.T. are supported by the United States National Science Foundation (NSF) grants AST-1911225 and AST-1911151. A.B. and E.R.C. acknowledge support from the National Aeronautics and Space Administration (NASA) through the Neil Gehrels Swift Guest Investigator Program (proposal number 1922148). Additional support for A.B. was provided by NASA through Chandra award number 25700383 issued by the Chandra X-ray Observatory Center, which is operated by the Smithsonian Astrophysical Observatory for and on behalf of NASA under contract NAS8-03060, and by NASA through the FINESST program, grant 80NSSC24K1548. E.R.C. acknowledges additional support from the NSF through grant AST-2006684 and from NASA through the Astrophysics Theory Program (grant No. 80NSSC24K0897). I.L. acknowledges support from a Rothschild Fellowship, the Gruber Foundation, and a Simons Investigator grant (No. 827103). A.H. is grateful for support by the BSF (grant No. 2020203), the ISF (grant No. 1679/23), and the Sir Zelman Cowen Universities Fund. C.J.N. acknowledges support from the Science and Technology Facilities Council (grant No. ST/Y000544/1) and the Leverhulme Trust (grant No. RPG-2021-380). K.D.F. acknowledges support from NSF grant AST-2206164. A.Z. acknowledges support by the BSF (grant No. 2020750), the NSF (grant No. 2109066), the Ministry of Science and Technology, Israel, and the ISF (grant No. 864/23). P.C. acknowledges support via the Research Council of Finland (grant No. 340613). M.J.D. is

funded by the UK Science and Technology Facilities Council (STFC) as part of the Gravitational-wave Optical Transient Observer (GOTO) project (grant No. ST/V000853/1). J.L., M. P., and D.O. acknowledge support from a UK Research and Innovation Fellowship (MR/T020784/1).

This work makes use of data from the Las Cumbres Observatory global telescope network. This Letter includes data collected by the TESS mission, which are publicly available from the Mikulski Archive for Space Telescopes (MAST). Funding for the TESS mission is provided by NASA’s Science Mission Directorate. We acknowledge the staff who operate and run the AMI-LA telescope at Lord’s Bridge, Cambridge, for the AMI-LA radio data. AMI is supported by the Universities of Cambridge and Oxford and by the European Research Council under grant ERC-2012-StG-307215 LODESTONE. We thank the National Radio Astronomy Observatory (NRAO) for carrying out the Karl G. Jansky Very Large Array (VLA) observations.

ORCID iDs

Lydia Makrygianni  <https://orcid.org/0000-0002-7466-4868>
 Iair Arcavi  <https://orcid.org/0000-0001-7090-4898>
 Megan Newsome  <https://orcid.org/0000-0001-9570-0584>
 Ananya Bandopadhyay  <https://orcid.org/0000-0002-5116-844X>
 Eric R. Coughlin  <https://orcid.org/0000-0003-3765-6401>
 Itai Linial  <https://orcid.org/0000-0002-8304-1988>
 Brenna Mockler  <https://orcid.org/0000-0001-6350-8168>
 Eliot Quataert  <https://orcid.org/0000-0001-9185-5044>
 Chris Nixon  <https://orcid.org/0000-0002-2137-4146>
 Benjamin Godson  <https://orcid.org/0000-0003-3766-7266>
 Miika Pursiainen  <https://orcid.org/0000-0003-4663-4300>
 Giorgos Leloudas  <https://orcid.org/0000-0002-8597-0756>
 K. Decker French  <https://orcid.org/0000-0002-4235-7337>
 Adi Zitrin  <https://orcid.org/0000-0002-0350-4488>
 Sara Faris  <https://orcid.org/0009-0007-8485-1281>
 Marco C. Lam  <https://orcid.org/0000-0002-9347-2298>
 Assaf Horesh  <https://orcid.org/0000-0002-5936-1156>
 Itai Sfaradi  <https://orcid.org/0000-0003-0466-3779>
 Michael Fausnaugh  <https://orcid.org/0000-0002-9113-7162>
 Ehud Nakar  <https://orcid.org/0000-0002-4534-7089>
 Kendall Ackley  <https://orcid.org/0000-0002-8648-0767>
 Moira Charalampopoulos  <https://orcid.org/0000-0002-1895-6639>
 Panos Charalampopoulos  <https://orcid.org/0000-0002-0326-6715>
 Benjamin D. R. Davies  <https://orcid.org/0009-0000-5659-9006>
 Yael Dgany  <https://orcid.org/0000-0002-7579-1105>
 Martin J. Dyer  <https://orcid.org/0000-0003-3665-5482>
 Joseph Farah  <https://orcid.org/0000-0003-4914-5625>
 David A. Green  <https://orcid.org/0000-0003-3189-9998>
 D. Andrew Howell  <https://orcid.org/0000-0003-4253-656X>
 Thomas Killestein  <https://orcid.org/0000-0002-0440-9597>
 Niilo Koivisto  <https://orcid.org/0009-0007-7151-7313>
 Joseph Lyman  <https://orcid.org/0000-0002-3464-0642>
 Curtis McCully  <https://orcid.org/0000-0001-5807-7893>
 Morgan A. Mitchell  <https://orcid.org/0009-0004-6130-7775>
 Estefania Padilla Gonzalez  <https://orcid.org/0000-0003-0209-9246>
 Lauren Rhodes  <https://orcid.org/0000-0003-2705-4941>
 Giacomo Terreran  <https://orcid.org/0000-0003-0794-5982>
 Ben Warwick  <https://orcid.org/0009-0005-8379-3871>

References

- Abolfathi, B., Aguado, D. S., Aguilar, G., et al. 2018, *ApJS*, 235, 42
- Aguado, D. S., Ahumada, R., Almeida, A., et al. 2019, *ApJS*, 240, 23
- Alard, C., & Lupton, R. H. 1998, *ApJ*, 503, 325
- Alexander, K. D., Berger, E., Guillochon, J., Zauderer, B. A., & Williams, P. K. G. 2016, *ApJL*, 819, L25
- Arcavi, I. 2022, *ApJ*, 937, 75
- Arcavi, I., Dgany, Y., Makrygianni, L., & Pellegrino, C. 2022, *TNSAN*, 47, 1
- Arcavi, I., Gal-Yam, A., Sullivan, M., et al. 2014, *ApJ*, 793, 38
- Bahcall, J. N., & Wolf, R. A. 1977, *ApJ*, 216, 883
- Bandopadhyay, A., Coughlin, E. R., Nixon, C. J., & Pasham, D. R. 2024, *ApJ*, 974, 80
- Barniol Duran, R., Nakar, E., & Piran, T. 2013, *ApJ*, 772, 78
- Becker, A. 2015 HOTPANTS: High Order Transform of PSF ANd Template Subtraction. Astrophysics Source Code Library, ascl:1504.004
- Bellm, E. C., Kulkarni, S. R., Barlow, T., et al. 2019, *PASP*, 131, 068003
- Blagorodnova, N., Cenko, S. B., Kulkarni, S. R., et al. 2019, *ApJ*, 873, 92
- Blagorodnova, N., Gezari, S., Hung, T., et al. 2017, *ApJ*, 844, 46
- Bowen, I. S. 1928, *ApJ*, 67, 1
- Brinchmann, J., Charlot, S., White, S. D. M., et al. 2004, *MNRAS*, 351, 1151
- Brown, T. M., Baliber, N., Bianco, F. B., et al. 2013, *PASP*, 125, 1031
- Burrows, D. N., Hill, J. E., Nousek, J. A., et al. 2005, *SSRv*, 120, 165
- Cannizzaro, G., Wevers, T., Jonker, P. G., et al. 2021, *MNRAS*, 504, 792
- Cannizzo, J. K., Lee, H. M., & Goodman, J. 1990, *ApJ*, 351, 38
- Cendes, Y., Berger, E., Alexander, K. D., et al. 2022, *ApJ*, 938, 28
- Charalampopoulos, P., Leloudas, G., Malesani, D. B., et al. 2022, *A&A*, 659, A34
- Charalampopoulos, P., Pursiainen, M., Leloudas, G., et al. 2023, *A&A*, 673, A95
- Chen, X., Madau, P., Sesana, A., & Liu, F. K. 2009, *ApJL*, 697, L149
- Chevalier, R. A. 1998, *ApJ*, 499, 810
- Coughlin, E. R., & Armitage, P. J. 2018, *MNRAS*, 474, 3857
- Coughlin, E. R., Armitage, P. J., Nixon, C., & Begelman, M. C. 2017, *MNRAS*, 465, 3840
- Coughlin, E. R., & Nixon, C. J. 2019, *ApJL*, 883, L17
- Coughlin, E. R., & Nixon, C. J. 2022, *MNRAS*, 517, L26
- Cufari, M., Coughlin, E. R., & Nixon, C. J. 2022, *ApJL*, 929, L20
- Cufari, M., Nixon, C. J., & Coughlin, E. R. 2023, *MNRAS*, 520, L38
- Cutri, R. M., Wright, E. L., Conrow, T., et al. 2021, *yCat*, II/328
- Dai, L., McKinney, J. C., Roth, N., Ramirez-Ruiz, E., & Miller, M. C. 2018, *ApJL*, 859, L20
- Darbha, S., Coughlin, E. R., Kasen, D., & Quataert, E. 2018, *MNRAS*, 477, 4009
- Demircan, O., & Kahraman, G. 1991, *Ap&SS*, 181, 313
- Dgany, Y., Arcavi, I., Makrygianni, L., Pellegrino, C., & Howell, D. A. 2023, *ApJ*, 957, 57
- Faris, S., Arcavi, I., Makrygianni, L., et al. 2024, *ApJ*, 969, 104
- Fausnaugh, M. M., Valley, P. J., Kochanek, C. S., et al. 2021, *ApJ*, 908, 51
- French, K. D., Arcavi, I., & Zabludoff, A. 2016, *ApJL*, 818, L21
- French, K. D., Arcavi, I., & Zabludoff, A. 2017, *ApJ*, 835, 176
- French, K. D., Wevers, T., Law-Smith, J., Graur, O., & Zabludoff, A. I. 2020, *SSRv*, 216, 32
- French, K. D., & Zabludoff, A. I. 2018, *ApJ*, 868, 99
- Gehrels, N., Chincarini, G., Giommi, P., et al. 2004, *ApJ*, 611, 1005
- Gezari, S. 2021, *ARA&A*, 59, 21
- Gezari, S., Chornock, R., Rest, A., et al. 2012, *Natur*, 485, 217
- Goicovic, F. G., Springel, V., Ohlmann, S. T., & Pakmor, R. 2019, *MNRAS*, 487, 981
- Golightly, E. C. A., Nixon, C. J., & Coughlin, E. R. 2019, *ApJL*, 882, L26
- Guillochon, J., Manukian, H., & Ramirez-Ruiz, E. 2014, *ApJ*, 783, 23
- Guillochon, J., Nicholl, M., Villar, V. A., et al. 2018, *ApJS*, 236, 6
- Guillochon, J., & Ramirez-Ruiz, E. 2013, *ApJ*, 767, 25
- Guolo, M., Gezari, S., Yao, Y., et al. 2024, *ApJ*, 966, 160
- Hammerstein, E., van Velzen, S., Gezari, S., et al. 2023, *ApJ*, 942, 9
- Hayasaki, K., Zhong, S., Li, S., Berczik, P., & Spurzem, R. 2018, *ApJ*, 855, 129
- Henden, A. A., Templeton, M., Terrell, D., et al. 2016, *yCat*, II/336
- Hickish, J., Razavi-Ghods, N., Perrott, Y. C., et al. 2018, *MNRAS*, 475, 5677
- Hills, J. G. 1988, *Natur*, 331, 687
- Hinkle, J. T., Auchettl, K., Hoogendam, W. B., et al. 2024, arXiv:2412.15326
- Holoien, T. W. S., Kochanek, C. S., Prieto, J. L., et al. 2016, *MNRAS*, 455, 2918
- Holoien, T. W. S., Prieto, J. L., Bersier, D., et al. 2014, *MNRAS*, 445, 3263
- Horesh, A., Cenko, S. B., & Arcavi, I. 2021a, *NatAs*, 5, 491
- Horesh, A., Sfaradi, I., Fender, R., et al. 2021b, *ApJL*, 920, L5
- Home, K. 1986, *PASP*, 98, 609
- Hung, T., Gezari, S., Blagorodnova, N., et al. 2017, *ApJ*, 842, 29
- Jarrett, T. H., Chester, T., Cutri, R., et al. 2000, *AJ*, 119, 2498
- Jiang, Y.-F., Guillochon, J., & Loeb, A. 2016, *ApJ*, 830, 125
- Kauffmann, G., Heckman, T. M., White, S. D. M., et al. 2003, *MNRAS*, 341, 33
- Kormendy, J., & Ho, L. C. 2013, *ARA&A*, 51, 511
- Kozai, Y. 1962, *AJ*, 67, 591
- Krolik, J., Piran, T., & Ryu, T. 2020, *ApJ*, 904, 68
- Lacy, J. H., Townes, C. H., & Hollenbach, D. J. 1982, *ApJ*, 262, 120
- Lam, M. C., & Smith, R. J. 2022, ASPIRED: A Python-based Spectral Data Reduction Toolkit, v0.4.6, Zenodo, doi:10.5281/zenodo.6903357
- Lam, M. C., Smith, R. J., Arcavi, I., et al. 2023, *AJ*, 166, 13
- Leja, J., Johnson, B. D., Conroy, C., van Dokkum, P. G., & Byler, N. 2017, *ApJ*, 837, 170
- Leloudas, G., Dai, L., Arcavi, I., et al. 2019, *ApJ*, 887, 218
- Lidov, M. L. 1962, *P&SS*, 9, 719
- Lin, Z., Jiang, N., Wang, T., et al. 2024, *ApJL*, 971, L26
- Linial, I., & Quataert, E. 2024, *MNRAS*, 527, 4317
- Liu, C., Yarza, R., & Ramirez-Ruiz, E. 2025, *ApJ*, 979, 40
- Lodato, G., King, A. R., & Pringle, J. E. 2009, *MNRAS*, 392, 332
- Mainzer, A., Bauer, J., Cutri, R. M., et al. 2014, *ApJ*, 792, 30
- Mainzer, A., Bauer, J., Grav, T., et al. 2011, *ApJ*, 731, 53
- Makrygianni, L., Trakhtenbrot, B., Arcavi, I., et al. 2023, *ApJ*, 953, 32
- McConnell, N. J., Ma, C.-P., Gebhardt, K., et al. 2011, *Natur*, 480, 215
- Melchor, D., Mockler, B., Naoz, S., Rose, S. C., & Ramirez-Ruiz, E. 2024, *ApJ*, 960, 39
- Merritt, D. 2000, in ASP Conf. Ser. 197, Dynamics of Galaxies: From the Early Universe to the Present, ed. F. Combes, G. A. Mamon, & V. Charmandaris (San Francisco, CA: ASP), 221
- Merritt, D. 2013, Dynamics and Evolution of Galactic Nuclei (Princeton, NJ: Princeton Univ. Press)
- Mockler, B., Guillochon, J., & Ramirez-Ruiz, E. 2019, *ApJ*, 872, 151
- Mockler, B., & Ramirez-Ruiz, E. 2021, *ApJ*, 906, 101
- Nasa High Energy Astrophysics Science Archive Research Center (Heasarc), 2014 HEASoft: Unified Release of FTOOLS and XANADU, Astrophysics Source Code Library, ascl:1408.004
- Netzer, H., Elitzur, M., & Ferland, G. J. 1985, *ApJ*, 299, 752
- Nicholl, M. 2018, *RNAAS*, 2, 230
- Nicholl, M., Blanchard, P. K., Berger, E., et al. 2019, *MNRAS*, 488, 1878
- Nicholl, M., Lanning, D., Ramsden, P., et al. 2022, *MNRAS*, 515, 5604
- Nicholl, M., Wevers, T., Oates, S. R., et al. 2020, *MNRAS*, 499, 482
- Norman, S. M. J., Nixon, C. J., & Coughlin, E. R. 2021, *ApJ*, 923, 184
- Onori, F., Cannizzaro, G., Jonker, P. G., et al. 2019, *MNRAS*, 489, 1463
- Paxton, B., Bildsten, L., Dotter, A., et al. 2011, *ApJS*, 192, 3
- Payne, A. V., Shappee, B. J., Hinkle, J. T., et al. 2021, *ApJ*, 910, 125
- Perrott, Y. C., Scaife, A. M. M., Green, D. A., et al. 2013, *MNRAS*, 429, 3330
- Peters, P. C. 1964, *PhRv*, 136, 1224
- Phinney, E. S. 1989, in IAU Symp. 136, The Center of the Galaxy, ed. M. Morris (Dordrecht: Kluwer), 543
- Piran, T., Svirski, G., Krolik, J., Cheng, R. M., & Shiokawa, H. 2015, *ApJ*, 806, 164
- Price, D. J., Wurster, J., Tricco, T. S., et al. 2018, *PASA*, 35, e031
- Prochaska, J. X., Hennawi, J. F., Westfall, K. B., et al. 2020, *JOSS*, 5, 2308
- Quinlan, G. D. 1996, *NewA*, 1, 35
- Ramsden, P., Lanning, D., Nicholl, M., & McGee, S. L. 2022, *MNRAS*, 515, 1146
- Rees, M. J. 1988, *Natur*, 333, 523
- Ricarte, A., Natarajan, P., Dai, L., & Coppi, P. 2016, *MNRAS*, 458, 1712
- Ricker, G. R., Winn, J. N., Vanderspek, R., et al. 2015, *JATIS*, 1, 014003
- Roming, P. W. A., Kennedy, T. E., Mason, K. O., et al. 2005, *SSRv*, 120, 95
- Roth, N., Kasen, D., Guillochon, J., & Ramirez-Ruiz, E. 2016, *ApJ*, 827, 3
- Ryu, T., Krolik, J., & Piran, T. 2020a, *ApJ*, 904, 73
- Ryu, T., Krolik, J., Piran, T., & Noble, S. C. 2020b, *ApJ*, 904, 100
- Sand, D. J., Brown, T., Haynes, R., & Dubberley, M. 2011, AAS Meeting, 218, 132.03
- Saxton, R., Komossa, S., Auchettl, K., & Jonker, P. G. 2021, *SSRv*, 217, 18
- Schneider, P., Ehlers, J., & Falco, E. E. 1992, Gravitational Lenses (Berlin: Springer-Verlag)
- Seibert, M., Wyder, T., Neill, J., et al. 2012, AAS Meeting, 219, 340.01
- Sfaradi, I., Beniamini, P., Horesh, A., et al. 2024, *MNRAS*, 527, 7672
- Sfaradi, I., Horesh, A., Fender, R., et al. 2022, *ApJ*, 933, 176
- Shappee, B. J., Prieto, J. L., Grupe, D., et al. 2014, *ApJ*, 788, 48
- Somalwar, J. J., Ravi, V., & Lu, W. 2025a, *ApJ*, 983, 159
- Somalwar, J. J., Ravi, V., Yao, Y., et al. 2025b, *ApJ*, 985, 175
- Speagle, J. S. 2020, *MNRAS*, 493, 3132

- Stanek, K. Z. 2022, TNSTR, [2022-1433](#), 1
- Steehgs, D., Galloway, D. K., Ackley, K., et al. 2022, [MNRAS](#), **511**, 2405
- Steinberg, E., Coughlin, E. R., Stone, N. C., & Metzger, B. D. 2019, [MNRAS](#), **485**, L146
- Stone, N. C., Kesden, M., Cheng, R. M., & van Velzen, S. 2019, [GReGr](#), **51**, 30
- Stone, N. C., Vasiliev, E., Kesden, M., et al. 2020, [SSRv](#), **216**, 35
- Sun, J., Guo, H., Gu, M., et al. 2025, [ApJ](#), **982**, 150
- Tonry, J. L., Denneau, L., Heinze, A. N., et al. 2018, [PASP](#), **130**, 064505
- Trakhtenbrot, B., Arcavi, I., Ricci, C., et al. 2019, [NatAs](#), **3**, 242
- Tremonti, C. A., Heckman, T. M., Kauffmann, G., et al. 2004, [ApJ](#), **613**, 898
- Valenti, S., Howell, D. A., Stritzinger, M. D., et al. 2016, [MNRAS](#), **459**, 3939
- van Velzen, S. 2018, [ApJ](#), **852**, 72
- van Velzen, S., Farrar, G. R., Gezari, S., et al. 2011, [ApJ](#), **741**, 73
- van Velzen, S., Gezari, S., Hammerstein, E., et al. 2021, [ApJ](#), **908**, 4
- van Velzen, S., Holoiien, T. W. S., Onori, F., Hung, T., & Arcavi, I. 2020, [SSRv](#), **216**, 124
- Veitch-Michaelis, J., & Lam, M. C. 2020, in ASP Conf. Ser. 527, Astronomical Data Analysis Software and Systems XXIX, ed. R. Pizzo et al. (San Francisco, CA: ASP), 627
- Veitch-Michaelis, J., & Lam, M. C. 2021, Rascal, v0.3.0, Zenodo, doi:[10.5281/zenodo.4124170](#)
- Veres, P. M., Franckowiak, A., van Velzen, S., et al. 2024, arXiv:[2408.17419](#)
- Wegg, C., & Nate Bode, J. 2011, [ApJL](#), **738**, L8
- Wen, S., Jonker, P. G., Levan, A. J., et al. 2024, [ApJ](#), **970**, 116
- Wevers, T., Coughlin, E. R., Pasham, D. R., et al. 2023, [ApJL](#), **942**, L33
- Wevers, T., Pasham, D. R., van Velzen, S., et al. 2019, [MNRAS](#), **488**, 4816
- Yao, Y., Chornock, R., LeBaron, N., et al. 2024, TNSAN, **43**, 1
- Yao, Y., Ravi, V., Gezari, S., et al. 2023, [ApJL](#), **955**, L6
- Zwart, J. T. L., Barker, R. W., Biddulph, P., et al. 2008, [MNRAS](#), **391**, 1545